

UCLA

UCLA Electronic Theses and Dissertations

Title

Auxiliary system to overcome resistance of therapeutic monoclonal antibody in anti-cancer treatment

Permalink

<https://escholarship.org/uc/item/51729015>

Author

Qi, Tong

Publication Date

2024

Peer reviewed|Thesis/dissertation

UNIVERSITY OF CALIFORNIA

Los Angeles

Auxiliary system to overcome resistance of therapeutic monoclonal antibody in anti-
cancer treatment

A dissertation submitted in partial satisfaction of the requirements for the degree Doctor
of Philosophy in Chemical Engineering

by

Tong Qi

2024

© Copyright by

Tong Qi

2024

ABSTRACT OF THE DISSERTATION

Auxiliary system to overcome resistance of therapeutic monoclonal antibody in anti-cancer treatment

by

Tong Qi

Doctor of Philosophy in Chemical Engineering

University of California, Los Angeles, 2024

Professor Yunfeng Lu, Chair

Rituximab, an anti-CD20 monoclonal antibody, has revolutionized the treatment for lymphoma, particularly B-cell non-Hodgkin lymphoma; the therapeutic efficacy, however, is limited by its temporary activity, non-ideal biodistribution, and heterogeneity of the cancer cells. In this dissertation research, two auxiliary systems were designed to improve the therapeutic efficacy of rituximab. The first system involves a novel combination treatment for non-Hodgkin lymphoma using rituximab and a whole cell-based therapeutic cancer vaccine, which effectively elicited a specific immune response, established immune memory, offered both immediate tumor killing and sustained protection from relapse of cancer. The second system involves a design of novel protein delivery systems that target lymph nodes, which help eliminate circulating cancer cells within the lymph nodes, block metastatic pathways, and reduce cancer metastasis and

relapse. The strategies described in this dissertation research can be extended to other monoclonal antibody therapeutics and cancer therapies beyond non-Hodgkin lymphoma therapeutics, providing a platform towards more effective cancer therapy.

The dissertation of Tong Qi is approved.

Jun Chen

Dante A. Simonetti

Yi Tang

Yunfeng Lu, Committee Chair

University of California, Los Angeles 2024

Table of contents

Chapter 1: Lymphoma Overview: Global Impact and Current Rituximab's Therapeutic Advances..... 1

 1.1 Lymphoma epidemiology..... 1

 1.2 Current monoclonal antibody treatment. 1

Chapter 2: Enhancing Monoclonal Antibody Therapy through Synergistic Tumor Vaccination..... 4

 2.1 Introduction..... 4

 2.1.1 Passive and active immunity..... 4

 2.1.2 Current art of cancer vaccine and synergy treatment of adoptive immunotherapy with monoclonal antibody. 5

 2.2 Materials and methods. 8

 2.2.1 Materials. 8

 2.2.2 Instruments..... 9

 2.2.3 Cell culture..... 9

 2.2.4 Lymphoma model setup and progression monitoring *in vivo*. 10

 2.2.5 Cell silicification.....11

 2.2.6 Optical microscopy. 12

 2.2.7 Zeta-potential and size measurements. 12

 2.2.8 Dendritic cells (DCs) internalization *in vitro*..... 12

2.2.9 DC activation in vitro.....	13
2.2.10 DC specific functional studies in vitro and in vivo.....	13
2.2.11 Vaccination of silicified cells in BLT humanized mice.....	14
2.2.12 CD8 positive T cell killing assay.	14
2.2.13 Systemic toxicity.....	15
2.2.14 Statistics.	15
2.3 Results.....	15
2.3.1 Rituximab treatment is insufficient to eliminate lymphoma.....	15
2.3.2 The therapeutic vaccine is successfully synthesized through cryo-silicification of lymphoma.	18
2.3.3 TLR agonist modification on the cryo-silicification of lymphoma prompts uptake and activation of dendritic cells.	21
2.3.4 The combination treatment of RTX and cryo-silicification of lymphoma inhibits lymphoma progression in xenograft humanized BLT mice.	24
2.3.5 The combination treatment improves activation of effector cells and induction of memory cells in CD8+ T cells.....	28
2.3.6 The combination treatment provides specific protection from tumor growth.	31
2.3.7 The combination treatment prevents tumor relapse.....	34
2.3.8 The combination treatment exhibits a biosafety profile.	37

2.4 Conclusion and discussion.....	38
Chapter 3: Advancing Monoclonal Antibody Therapy with Targeted Delivery to Lymph Nodes.....	41
3.1 Introduction.....	41
3.1.1 Metastatic pathway and physiology of lymphatic system.	41
3.1.2 Current art of lymph-node targeting nanoparticles.....	47
3.1.3 Nanoencapsulation platform for enhanced efficacy of protein therapeutics.....	48
3.1.4 Development of a novel LN-delivery nanocapsule targeting high endothelial venules (HEVs).....	50
3.2 Materials and methods.....	52
3.2.1 Materials.....	52
3.2.2 Instruments.....	52
3.2.3 Synthesis of RTX nanocapsule.....	53
3.2.4 Determination of protein concentration.....	54
3.2.5 Synthesis of nanocapsules conjugated with MECA-79.....	54
3.2.6 Determination of average number of conjugated ligands on nanocapsules.	54
3.2.7 Zeta-potential and size measurement.....	55
3.2.8 Cell culture.....	55

3.2.9 Lymphoma model setup and progression monitoring in vivo.	56
3.2.10 Biodistribution studies.	56
3.2.11 Pharmacokinetics studies.	57
3.2.12 Monoclonal antibody detection by ELISA.	57
3.2.13 Cytotoxicity assay.	58
3.2.14 Anti-tumor efficacy of RTX in murine lymphoma model.	58
3.2.15 Metabolic pathway analysis.	59
3.2.16 Anti-tumor efficacy of RTX in human lymphoma model in mice.	59
3.2.17 Systemic toxicity.	60
3.2.18 Statistics.	60
3.3 Results.	60
3.3.1 MECA-79 modified nanocapsule induces specific accumulation in Lymph nodes.	60
3.3.2 Encapsulation and surface modification retains the anti-tumor efficacy of monoclonal antibody.	64
3.3.3 MECA-79 modified nanocapsules suppress tumor progression and obstruct lymph-node mediated metastasis.	67
3.3.4 MECA-79 modified nanocapsules inhibit human non-Hodgkin lymphoma progression.	72
3.3.5 Modified nanocapsules exhibit a biosafety profile.	75

3.4 Conclusion and discussion.....	76
Chapter 4: Summarization and perspective.	79
Reference.	82

Chapter 1: Lymphoma Overview: Global Impact and Current Rituximab's Therapeutic Advances.

1.1 Lymphoma epidemiology.

Lymphomas are a heterogeneous group of malignancies that arise from the clonal proliferation of B- cell, T- cell, and natural killer (NK) cell subsets at different maturation stages. The two main types of lymphomas are Hodgkin lymphoma (HL) and non-Hodgkin lymphoma (NHL), with the latter accounting for over 85% of cases¹. Each subtype presents unique epidemiological profiles, etiological factors, and clinical outcomes. The global impact of lymphoma is profound, affecting populations worldwide with significant variability in incidence, prognosis, and survival rates based on geographic and demographic factors. NHL is the most common hematopoietic malignancy in the United States, representing nearly 4% of all cancer cases and deaths. Particularly, the prognosis for patients is extremely poor when this malignancy, primary or metastatic, develops in the central nervous system (CNS). In the United States, it ranks as the seventh most common cancer and the sixth in cancer mortality, with approximately 85% of NHL cases being B-cell lymphomas. The American Cancer Society's estimates for NHL in 2024 suggest that approximately 80,620 people will be diagnosed, and about 20,140 will die from this cancer in the United States alone. This includes both adults and children, highlighting the significant impact of NHL on public health.

1.2 Current monoclonal antibody treatment.

The most important advance in the treatment of B-NHL in the past three decades was the addition of rituximab (RTX) to the standard chemotherapy regimen, which

significantly improves treatment outcomes in clinics^{2, 3}. RTX is routinely included in all phases of conventional treatment, such as first-line therapy, maintenance, and salvage therapy^{4, 5}. However, the effectiveness of rituximab is still limited by the development of treatment resistance like other antineoplastic agents. Unlike conventional chemotherapeutic agents, mechanisms of tumor resistance have been clearly elucidated. Treatment resistance induced by rituximab is not purely due to tumor-specific alterations, as the action mechanisms of rituximab depend on not only cancer cell features, but also the activation of the host immune system^{6, 7}.

Rituximab is a chimeric monoclonal antibody derived from both mouse and human sources. It includes a human kappa constant region and a human IgG1 Fc portion, as well as a murine variable region that specifically targets the human CD20 antigen⁸. When rituximab binds to CD20, it leads to the reduction of both normal and malignant B cells. Unlike monoclonal antibodies that are conjugated to radioisotopes or immunotoxins, rituximab does not contain any additional "payload" for enhanced effect. Its action is driven entirely by its interaction with the CD20 antigen and the subsequent engagement with the immune system's components. Researchers have identified at least four major mechanisms through which rituximab depletes B cells. These mechanisms include apoptosis, complement-dependent cytotoxicity (CDC), antibody-dependent cellular cytotoxicity (ADCC), and antibody-dependent cellular-phagocytosis (ADCP)⁹⁻¹³. Compared with standard CHOP (cyclophosphamide, vincristine, doxorubicin, and prednisolone) chemotherapy, the RTX+CHOP combination therapy significantly increased the complete response rate, improved overall survival, and decreased the rates of tumor relapse, especially in elderly patients^{14, 15}.

The exact mechanisms of rituximab remain poorly understood; however, potential mechanisms of treatment resistance have been described¹⁶. One of the main mechanisms of treatment resistance is loss of CD20. Some cell lines resistant to rituximab exhibit reduced CD20 levels¹⁷. This reduction in CD20 expression affects the organization of lipid rafts and subsequent signaling pathways, indicating that the relationship between CD20 expression and rituximab resistance involves more than just the ratios of antibody to antigen¹⁸. The initial findings of acquired mutations in the CD20 gene were documented in 2009, which discovered mutations that led to deletions in the C-terminal region of the CD20 gene in a group of tumor samples from patients with non-Hodgkin lymphoma (NHL)¹⁹.

The tumor microenvironment is increasingly recognized as a crucial factor in cancer biology and also influences the efficacy of rituximab^{20, 21}. The primary mechanism through which rituximab depletes B cells seems to vary with the microenvironment. Circulating B cells were eliminated through antibody-dependent cellular cytotoxicity in a human-CD20 transgenic mouse model, whereas B cells in the marginal zones of lymph nodes were predominantly destroyed via complement-dependent cytotoxicity²². Clinically, B cells are more readily depleted from the bloodstream by rituximab, whereas those in bone marrow and lymph nodes are more challenging and slower to clear²³. Therefore, treatment against different types of molecules expressed in B-NHL cells from RTX is necessary for effective treatment of B-NHL.

Chapter 2: Enhancing Monoclonal Antibody Therapy through Synergistic Tumor Vaccination.

2.1 Introduction.

2.1.1 Passive and active immunity.

Passive immunity and active immunity are two fundamental types of immunity that protect the body from pathogens²⁴. They play crucial roles in preventing and fighting infections but operate through different mechanisms and influence disease resistance^{25, 26}. Passive immunity refers to the type of immunity that is acquired through the transfer of antibodies from one individual to another²⁷. This can occur naturally, as in the case of antibodies in the placenta or breast milk from mother to newborn, providing the infant with immediate protection against certain infections^{28,29}. Passive immunity can also be acquired artificially, through the administration of monoclonal antibodies, such as Rituximab in lymphoma treatment^{30, 31}. In passive immunity, the recipient's immune system is not directly involved in producing new antibodies or immune cells, and it doesn't generate immune memory *in vivo*, which means once the transferred antibodies are degraded or the expression of surface proteins changes, protection provided by passive immunity will diminish or disappear³². On the other hand, active immunity is acquired when an individual is exposed to the pathogen, triggering the immune system to produce antibodies or activate cytotoxic lymphocytes against the pathogen^{33, 34}. Exposure to the pathogen can occur through infection with the actual disease pathogen (natural immunity), or through artificial introduction of a killed or weakened form of the disease organism via vaccination (vaccine induced immunity)³⁵⁻³⁷. Active immunity involves the recipient's immune system

recognizing the vaccine, producing tumor-specific effector cells and developing immunological memory, which may allow for a faster and more robust response upon re-exposure to the same pathogen. But it also takes a few weeks to develop active immunity so it cannot provide immediate protection (**Table 2-1**).

Table 2-1. Passive vs active immunity.

	Passive Immunity	Active Immunity
Source	Maternal antibodies Monoclonal antibodies	Infections Vaccines
Response time	Immediate	A few weeks
Immune system involvement	No	Yes
	Risk of off target	Tumor specific immune cells
Immune memory	No	Yes, long term protection

2.1.2 Current art of cancer vaccine and synergy treatment of adoptive immunotherapy with monoclonal antibody.

Cancer vaccine is a promising strategy to induce a specific and long-lasting immune response against tumor antigens, which are overexpressed proteins in tumor tissues and play an important role in tumor initiation, progression and metastasis^{38, 39}. In recent years, different types of cancer vaccines have been developed to generate an immune response, to eliminate the primary tumor and inhibit the potential relapse⁴⁰, including cell-based vaccines (dendritic cell vaccines^{41, 42} and whole tumor cell vaccines⁴³⁻⁴⁵), protein/peptide-based vaccines⁴⁶⁻⁴⁹, viral/bacterial-based vaccines⁵⁰⁻⁵⁴ and gene-based vaccines (RNA vaccines⁵⁵⁻⁵⁸ and DNA vaccines⁵⁹⁻⁶²). Different types of cancer vaccines have variable features (**Table 2-2**).

Table 2-2. Features of different types of cancer vaccines.

<p>Cell-based vaccines (dendritic cells/whole cancer cells)</p>	<p>Pros:</p> <ul style="list-style-type: none"> - High immunogenicity. - Control of antigen presentation.
<p>Protein/peptide-based vaccines</p>	<p>Cons:</p> <ul style="list-style-type: none"> - Difficult to mass produce.
<p>Protein/peptide-based vaccines</p>	<p>Pros:</p> <ul style="list-style-type: none"> - Low toxicity. - Easy to produce.
<p>Viral/bacterial-based vaccines</p>	<p>Cons:</p> <ul style="list-style-type: none"> - Moderate immunogenicity. - Restricted to the human leukocyte antigens (HLA)
<p>Viral/bacterial-based vaccines</p>	<p>Pros:</p> <ul style="list-style-type: none"> - High immunogenicity. - Easy to produce.
<p>Gene-based vaccines (RNA/DNA)</p>	<p>Cons:</p> <ul style="list-style-type: none"> - Potential high toxicity. - Risk of undesired infections.
<p>Gene-based vaccines (RNA/DNA)</p>	<p>Pros:</p> <ul style="list-style-type: none"> - Easy to deliver multiple antigens. - No restriction to HLA subtype.

	<p>Cons:</p> <ul style="list-style-type: none"> - Specific transportation and storage conditions. - Moderate immunogenicity in human.
--	---

Among all strategies, protein-based vaccines are promising for clinical applications with their low toxicity and easy manufacture, however, their wide application is hindered due to their limited immunogenicity. In order to increase the efficacy of protein-based vaccines, the Toll-like receptor (TLR) 3 and TLR7/8 are considered excellent adjuvant candidates⁶³⁻⁶⁶ to enhance the endocytosis and activation of DCs^{67, 68}, achieving a strong immune response of T cells. What's more, evidence in lymphoma patients suggests that a vaccinal effect can be generated by RTX treatment, resulting in durable responses after antibody concentration decreases⁶⁹. Moreover, anti-tumor cellular immune responses have been demonstrated after antibody treatment both in mouse models and patients⁷⁰⁻⁷². RTX opsonizes tumor cells and targets them for killing by FcγR-mediated ADCC, a process that generates antibody: tumor antigen immune complexes, which engage and stimulate dendritic cell (DC) maturation and presentation of tumor antigens to T cells^{70, 73}. Based on the crosstalk between RTX and the cellular immune response, RTX treatment in combination with adoptive immunotherapy with T cells that are cytotoxic to B-NHL cells has been considered as a powerful regimen with synergistic effect, allowing efficient travel and persistence of B-cell tumor-specific T cells at the site of the lesion^{74, 75}. Therefore, therapeutic cancer vaccines constructed from components or whole B-NHL cells can complement the efficacy of RTX by stimulating the adaptive immune system and

establishing long-term immunological memory against cancers with large amounts of a high-quality antigen and effective immune response.

Considering these findings, we developed a synergistic strategy for B-NHL with a combination treatment of RTX and a therapeutic vaccine. Briefly, therapeutic vaccines synthesized by TLR-agonist-modified cryo-silicification of B-NHL cells were evaluated in combination with RTX for their therapeutic efficacy against B-NHL. RTX treatment demonstrated effectively initial B-NHL depletion and improved trafficking of tumor-specific T cells to tumor sites. The therapeutic vaccines showed enhanced uptake and activation of dendritic cells. The combination treatment showed the synergistic and persistent effect of tumor antigen-specific cytotoxic T cells in effectively inhibiting B-NHL progression including the CNS metastasis and preventing tumor relapse.

2.2 Materials and methods.

2.2.1 Materials.

All chemicals were purchased from Sigma-Aldrich (St. Louis, MO) unless otherwise noted and were used as received. Resiquimod (R848) and poly(I:C) were purchased from InvivoGen (San Diego, CA). Polyethylenimine (PEI, linear, MW=25k) was purchased from Polysciences (Warrington, PA). Tetramethyl rhodamine (TAMRA) NHS ester was purchased from Lumiprobe (Hunt Valley, MD). Rituximab (RTX) was purchased from UCLA hospital pharmacy. Iscove's Modified Dulbecco's Medium (IMDM) and fetal bovine serum (FBS) were purchased from Corning (Corning, NY). Penicillin-streptomycin (PS) and zeocin were purchased from Thermo Fisher Scientific (West Hills, CA). REAlease CD8 Microbead kit was purchased from Miltenyi Biotec

(Auburn, CA). Matrigel was purchased from BD Biosciences (San Jose, CA). Anti-human CD3 (SK7), anti-human CD4 (OKT4), anti-human CD8 (SK1), anti-human CD11c (Bu15), anti-human CD44 (BJ18), anti-human CD45 (HI30), anti-human CD62L (DREG-56), anti-human CD69 (FN50), anti-human CD80 (2D10), anti-mouse H-2Kb bound to SIINFEKL Antibody (25-D1.16) were purchased from Biolegend (San Diego, CA). The ammonium–chloride–potassium (ACK) lysis buffer was purchased from quality biological (Gaithersburg, MD).

2.2.2 Instruments.

Images of cells and tissue sections were obtained with a Revolve R4 fluorescent microscope, Discover Echo Inc (San Diego, CA). Dynamic light scattering (DLS) studies of silicified cells were obtained by Zetasizer Nano instrument (Malvern Instruments Ltd., Kingdom). Biomarkers on cell surface were measured by Attune flow cytometer (Thermo Fisher Scientific) and cell sorting was achieved by BD FACSAria III cell sorter (BD Biosciences). Cell numbers were acquired by manual counting with trypan blue dye exclusion under microscope, or with MACSQuant Analyzer 10 (Miltenyi Biotech, Bergisch Gladbach Germany). Optical and bioluminescent images were collected on IVIS Lumina II In vivo imaging system (PerkinElmer, Inc, Waltham, MA).

2.2.3 Cell culture.

2F7-BR44 cell line was obtained from lab stock as previously described⁷⁶. Briefly, 2F7 cells were transduced with lentiviral vectors encoding mCherry and luciferase under ubiquitin C promoter. Transduced 2F7 cells were sorted, sub-cloned to obtain single cell clones and finally selected 2F7-BR44 single clone after in vivo selection for brain

metastasis lymphoma. 2F7-BR44 cells were cultured in IMDM with 15% FBS, 1% glutamine, 1% penicillin-streptomycin and 100 mg/ml zeocin at 37°C.

2.2.4 Lymphoma model setup and progression monitoring *in vivo*.

Animal research described in the study was approved by the University of California, Los Angeles' Chancellor's Animal Research Committee (Institutional Animal Care and Use Committee) and was conducted in accordance with guidelines for the housing and care of laboratory animals of the National Institutes of Health and Association for Assessment and Accreditation of Laboratory Animal Care International. Humanized mice were prepared as previously described⁷⁷⁻⁷⁹. Briefly, human fetal tissue was first purchased from Advanced Bioscience Resources without identifying information, which didn't require Institutional Review Board approval for its use. Busulfan (35 mg/kg) was injected intraperitoneally into NSG mice. Then, the mice were implanted with a portion of human fetal thymus combined with fetal liver derived CD34⁺ cells solidified in Matrigel under the kidney capsule. Peripheral blood was collected from retro-orbital sinus, to confirm reconstitution of human lymphocytes in mice. One million 2F7-BR44 cells were injected into BLT humanized mice via the lateral tail vein. Lymphoma formation and progression was monitored every week by IVIS Lumina II In Vivo Imaging System. Mice were anesthetized with isoflurane, and intraperitoneally injected with 3 mg luciferin (Pierce). Bioluminescent signals were obtained 5 minutes later. Tumor burden was quantified as the total photon flux per second within the region of interest (trunk area or head area).

2.2.5 Cell silicification.

Silicic acid solution was first prepared by mixing 10mM tetramethyl orthosilicate (TMOS), 100mM NaCl, 1mM HCl in deionized water. Ultrasound was applied to disperse TMOS in a hydrophilic solution⁸⁰. Silicic acid solution was left at room temperature for 2 hours, then stored at 4°C overnight and is ready to use. Cells were first collected and rinsed once with PBS and 0.9% saline (154 mM NaCl), respectively. Cells were spun down and resuspended with silicic acid solution, at the concentration of three million cells per milliliter. After incubating cells at room temperature for 10 minutes, the cell suspension was moved to -80°C overnight. Frozen cell suspension was thawed by placing it in an ice-water mixture, and then allowing it to incubate for 15 minutes after melting. Silicified cells were then purified with deionized water to remove uncoated cells, rinsed with PBS, and morphology was observed with microscope.

Silicified cells were coated with cationic polymer PEI for consequent surface modification. PEI stocking buffer (1 mg/ml) was prepared three days before use, by ultrasound dispersing PEI powder into deionized water for 5 minutes. Si cells were rinsed with deionized water and suspended with PEI working buffer (0.2 mg/ml) at the concentration of 5-10 million cells per milliliter. Incubate cell suspension at room temperature for 10 minutes and keep mix cells every minute, so that cells can be distributed evenly in solution and formed a uniform PEI coating on surface. PEI coated silicified cells were then rinsed three times with PBS solution and zeta potential was measured with Zetasizer Nano instrument.

Cationic polymer coated silicified cells were then modified with TLR agonists on the surface. Briefly, for dual introduction at the same time, 20 mg R848 and 50 mg

poly(I:C) was first diluted in cell-grade water and vortexed to well mixed. PEI coated silicified cells were rinsed with deionized water, suspended with TLR agonist solution, and incubated for 15 minutes. Modified silicified cells were then stocked at 4°C for further use.

2.2.6 Optical microscopy.

For bright field imaging of silicified cells, cells (5×10^6 cells/ml) were suspended in deionized water and imaged with Revolve R4 fluorescent microscope.

2.2.7 Zeta-potential and size measurements.

Zeta-potential and particle size were measured with Zetasizer Nano instrument. Cells were spun and resuspended in deionized water and measured three times for each group.

2.2.8 Dendritic cells (DCs) internalization in vitro.

To measure internalization in dendritic cells, silicified cells were first stained with propidium iodide (PI, 1 mg/ml) for 20 min. After incubation, PI-stained silicified cells were coated with PEI and modified as described above. Peripheral blood mononuclear cells (PBMCs) were purchased from UCLA/CFAR virology core, without any identifying information, including age, sex, ethnicity, or any other demographic data. Stained silicified cells with or without modification were added and incubated with PBMCs (silicified cells: PBMC = 10:1) overnight at 4°C. PBMC cells were then washed with PBS, blocked with 3% BSA solution for 15 min and labeled with anti-human CD11c in FACS buffer. Post 1 h incubation, cells were washed with PBS three times, fixed with 4% paraformaldehyde, and evaluated with Attune flow cytometer.

2.2.9 DC activation in vitro.

In vitro dendritic cells' activation was also studied. PBMCs were spun and resuspended with silicified cells at a ratio of silicified cells: PBMC = 10:1. After 24-hours incubation at 4°C, cells were blocked with 3% BSA solution, stained with anti-human CD11c and anti-human CD80 for 1 h. DC activation was then measured after fixation.

2.2.10 DC specific functional studies in vitro and in vivo.

Peripheral blood was collected from retro-orbital sinus from BALB/cJ mice. Blood was then incubated with ACK lysis buffer to remove red blood cells and to collect murine lymphocytes following instruction. 2F7-BR44 cells were transduced with a lentiviral vector encoding ovalbumin (OVA) and flow sorted for OVA expression on surface. 2F7-OVA cells were expanded, silicified, and modified as described above. Murine lymphocytes were incubated with silicified 2F7-OVA cells at a ratio of silicified cells: lymphocytes = 10:1. Cell suspension was mixed every 6 hours. Cells were then spun down, blocked, and labeled with fluorescent antibodies specific for CD11c and SIINFEKL-H2kb. Labeled cells were then analyzed using Attune flow cytometer.

BALB/cJ mice were used to measure DC function in vivo. Briefly, silicified 2F7-OVA cells were injected intravenously via lateral tail vein, with dose of 4×10^6 cells per mice in PBS. Blood was collected from mice after three days. Lymphocytes were then separated with ACK lysis buffer, blocked, and stained with fluorescent antibodies specific for CD11c and SIINFEKL-H2kb. Cells were then fixed and analyzed.

2.2.11 Vaccination of silicified cells in BLT humanized mice.

2F7-BR44 cells (1×10^6 cells per mouse) were injected intravenously via the lateral tail vein into reconstitution confirmed BLT humanized mice. Seven days after inoculation, mice were treated with a single dose of silicified cells (2×10^6 cells per mouse) or PBS Intraperitoneally on Day 7, 10, 21 and 24, as indicated group and schedule. Single treatment or combination therapy with RTX was administered with intravenous injection of RTX (12.5 mg/kg) on Day 7 in PBS solution. Mice were sacrificed when in a critical condition due to the lymphoma burden or at the end of timepoints predetermined in experimental design. After blood collection, mice were perfused with cold PBS and euthanized. Organs were then harvested and grounded into single-cell suspension. Isolated single cells from tissues were used to measure tumor burden, based on mCherry expression on 2F7-BR44 cells by flow cytometry.

2.2.12 CD8 positive T cell killing assay.

mCherry-transduced 2F7-BR44 cells (1×10^4 cells per well) and EGFP-transduced MT4 cells (1×10^4 cells per well) were seeded together in 96-well plate with 200 μ l culture medium. Spleen-derived CD8⁺T cells were purified with REAlease CD8 MicroBead Kit from spleen single cell suspension as indicated instruction manual. Isolated CD8⁺ T cells were then added to cancer cells at a ratio of effector cells: 2F7 tumor cells = 2:1. After overnight incubation, cancer cell viability was measured based on mCherry and EGFP expression by flow cytometry, and calculated as following formula:

$$\text{Cancer cell viability (\%)} = \frac{\text{2F7 cell counts}}{\text{MT4 cell counts}} \times 100\%$$

2.2.13 Systemic toxicity.

The major organs, including heart, liver, spleen, and lung were collected at endpoint and fixed in 4% paraformaldehyde for H&E histological analysis by UCLA Translational Pathology Core Laboratory.

2.2.14 Statistics.

Data are presented as means \pm S.D. unless otherwise indicated. Statistical significance was calculated using GraphPad Prism. The significance of survival curve data was compared by log-rank test. All the other comparisons of significance between groups were calculated by two-tailed unpaired t-test. The P values of 0.05 or less are considered significant.

2.3 Results.

2.3.1 Rituximab treatment is insufficient to eliminate lymphoma.

In order to validate the therapeutic efficacy of RTX against human lymphoma, we used the bone marrow-liver-thymus (BLT) humanized mice, where immunodeficient mice are reconstituted with a human immune system, to establish the lymphoma xenograft model with 2F7-BR44 cells—a single cell clone of parental 2F7 B-cell NHL isolated from the brain of xenografted immunodeficient mice⁷⁶. Specifically, a novel humanized BLT mouse model with an advanced immunodeficient NOD.Cg^{-Hc1} *Prkdc^{scid}Il2rg^{tm1Wjl}/SzJ* (NSG^{-Hc1}) mouse that lacks the common cytokine-receptor γ -chain (IL-2R γ) and has a corrected Hc gene for complement secretion was used. With the reconstitution of human immune cells, including T cells, B cells, natural killer cells and macrophages, differentiated from human hematopoietic stem/progenitor cells (HSPCs), NSG^{-Hc1}-BLT mice have been shown to

support all antibody function mechanisms of RTX relevant to clinic patients, including direct apoptosis, CDC, ADCC, or ADCP⁸¹. Moreover, the presence of functional complement is expected to synergize the pattern recognition receptor (PRR)-induced pathways in immune cells. However, RTX treatment shows insufficient efficacy against 2F7-BR44 with the CNS metastases in NSG^{-Hc1}-BLT mice. As shown in **Fig. 2-1 a**, **Fig. 2-1 b**, RTX treatment suppresses the growth of 2F7-BR44 but loses control of tumor growth mainly in the CNS. Moreover, the expression levels of CD20 on 2F7-BR44 cells were longitudinally monitored in blood weekly and detected in tumor resident organs, including the brain, bone marrow (BM), lymph nodes (LNs), and spleen, at the endpoints. Low counts of 2F7-BR44 were detected in peripheral blood when RTX was still detectable in blood; however, a significant downregulation of CD20 expression was observed within the same period (**Fig. 2-1 c**), resulting in tumor escape from RTX treatment. Interestingly, the expression levels of CD20 in tumors from different organs showed varied trends: stable expression levels were observed in tumors isolated from the brain, while a clear CD20-negative population emerged in tumors from other organs (**Fig. 2-1 c,d**). This suggests a lower concentration of RTX in the brain compared to that in other organs, as confirmed by ELISA assays (**Fig. 2-1 e**). Therefore, in combination of antibody treatment, a therapeutic vaccine, which is able to stimulate tumor antigen-specific cytotoxic T cells, was developed to achieve effective inhibition of lymphoma progression.

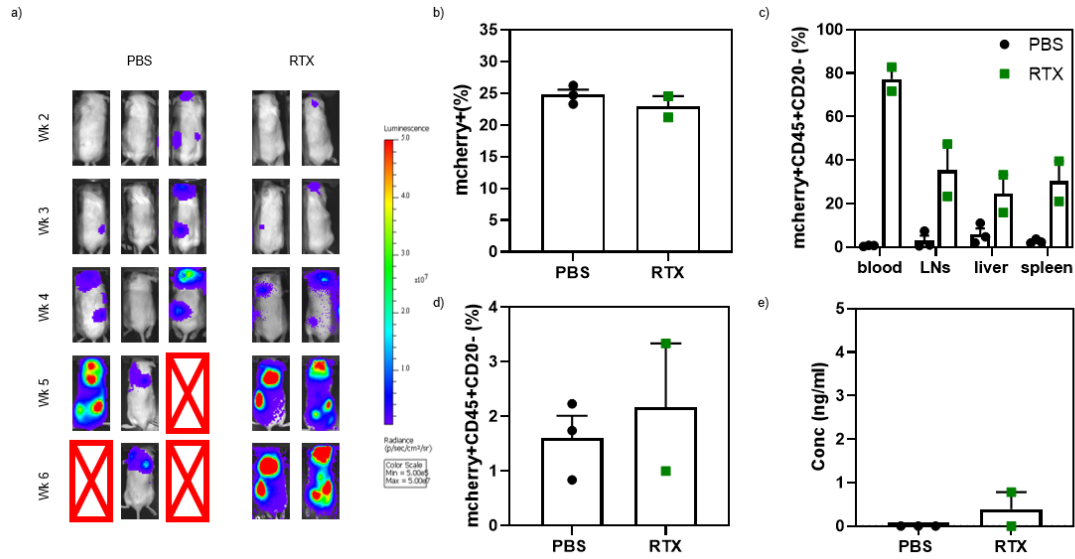


Fig. 2-1. RTX treatment alone is insufficient to eliminate lymphoma. 2F7-BR44 cells (1×10^6 cells per animal) were injected in humanized BLT mice after reconstitution confirmation. Mice were randomly separated into two groups for treatment with PBS or native RTX one week post engraftment. Treatments were administered intravenously through tail vein at 5 mg/kg/day for 5 days. **a**, Tumor progression was weekly tracked by bioluminescence imaging with In Vivo Imaging System. Sensitive settings were adjusted at each time point to maintain bioluminescence radiance at $5.00E5 - 5.00E7$ protons per pixel. **b**, Percentage of 2F7-BR44 cells in brain after RTX treatment was assessed by flow cytometry. **c**, Loss of CD20 expression on 2F7-BR44 cells in tissues. **d**, Loss of CD20 expression of 2F7-BR44 cells in brain area. **e**, Concentrations of RTX in perfused brain tissue at endpoint were measured by ELISA. Data are presented as means \pm S.E.M. LNs, lymph nodes.

2.3.2 The therapeutic vaccine is successfully synthesized through cryo-silicification of lymphoma.

Cryo-silicification, which encapsulates intact tumor cells in a delicate silica framework, can minimize artifacts by circumventing issues associated with chemical fixation and dehydration. This process prevents the formation of ice crystals, thus ensuring the preservation of cell integrity and surface protein contents. As shown in **Fig. 2-2 a**, we synthesized cryo-silicified 2F7-BR44 cells for lymphoma treatment through three steps as previously published⁸⁰. Briefly, we firstly doped silica on the surface of 2F7-BR44 to prepare si2F7 by suspending cells in a hypotonic aqueous solution of 100 mM NaCl and 10 mM tetramethyl orthosilicate (TMOS) at pH 3.0 for 10 min and then stored the mixed solution overnight at -80°C. Further surface modification was conducted to improve the efficacy. At physiological pH, hydroxyl (silanol Si-OH) groups on the cryo-silicified cell surface underwent dihydroxylation and transitioned to an anionic state (Si-O⁻), which enabled the adsorption of cationic molecules or polymers. Cationic polymer polyethyleneimine (PEI), which can recruit monocytes to the site of administration, enhance antigen uptake by antigen-presenting cells in intraperitoneal model, and has the ability to increase immunogenicity of DNA-based vaccines or nanoparticles as a TLR4 or TLR5 ligand^{59, 84}. In this study, si2F7-PEI was created by adsorbing PEI onto the surface of si2F7. Subsequently, these adsorbed PEI with positive charge served as a platform for further adsorption and retention of anionic ligands, including Toll-like receptor (TLR) agonists to bridge between innate and adaptive immunity and help to activate immune responses⁸⁵. Herein, resiquimod (R848), a TLR7/8 agonist, and poly(I:C), a TLR3 agonist were adsorbed on si2F7-PEI through electrostatic forces to form vac-si2F7, promoting antigen

internalization, enhancing antigen presentation to antigen-presenting cells (APCs), and stimulating robust and comprehensive immune response. These vac-si2F7 exhibited an intact and spherical morphology (**Fig. 2-2 b**) and a uniform size of approximately 10 μm (**Fig. 2-2 c**). Furthermore, the observed alterations in surface charge, transitioning from highly negative (si2F7) to positive (si2F7-PEI) due to PEI absorption, and subsequently reverting to almost neutral with the addition of R848 and poly(I:C) (vac-si2F7), clearly demonstrated the successful completion of each phase in the cryo-silicification process (**Fig. 2-2 d**). It's worth noting that the neutral charge and spherical structure eliminates systemic toxicity and increases dendritic cell uptake and also enhances *in vivo* accumulation to sites of large immune cell populations^{86, 87}. The vac-si2F7 was able to fully preserve the integrated cell structure, showing comparable cell size and internal complexity to living 2F7-BR44 cells by flow cytometry (**Fig. 2-2 e**).

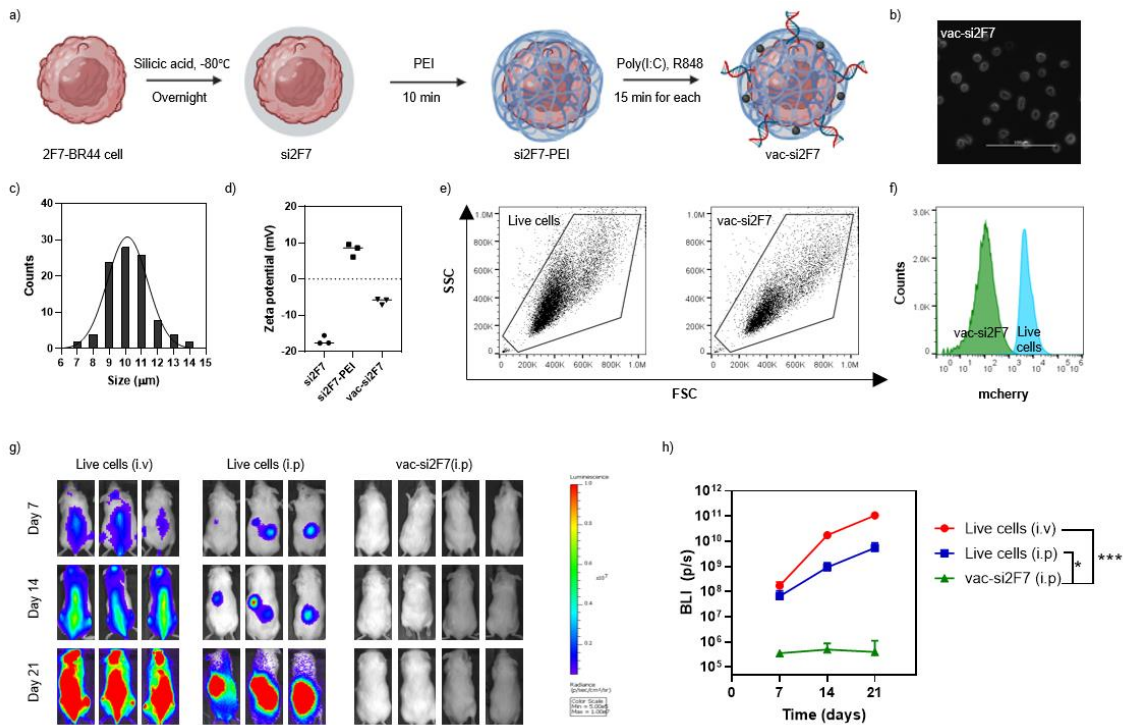


Fig. 2-2. Characterization of silicified cancer cells. **a**, Schematic of silicified cancer cell preparation. **b**, Microscope images of silicified cancer cells, with a spherical microscale architecture. **c**, Uniform diameter of silicified cells. **d**, Zeta-potential analysis of silicified cells with different surface modification (n=3). **e**, Representative flow cytometry dot plots of live cells and silicified cells exhibiting integrity in structure after silicification. **f**, Flow cytometry histogram analysis of mCherry transfected live cells and silicified cells, demonstrating silicified cells are non-viable. (n=3). **g**, In vivo imaging of mice injected with live cells or silicified cells, indicating silicified cells cannot generate tumor burden in vivo. **h**, Quantitative analysis of tumor burden over time based on IVIS bioluminescence (n=3 to 4). Data are presented as means \pm S.D. Statistical significance was calculated by t-test. *P<0.05, ***P<0.001.

Biosafety is a primary concern when utilizing whole cancer cells for therapeutic purposes. To address this, we conducted biosafety evaluations of cryo-silicified cells both *in vitro* and *in vivo*. For these studies, 2F7-BR44 cells were genetically modified using lentiviral vectors to express an mCherry-luciferase fusion protein, which was used as a marker to monitor cell viability. All vac-si2F7 cells lost their expression of mCherry (**Fig. 2-2 f**), indicating that these cells were non-viable after silicification due to impaired protein synthesis. To further confirm the loss of biological activity in silicified cells, NSG^{-Hc1} mice were xenografted either intraperitoneally (IP) or intravenously (IV) with living 2F7-BR44 cells or vac-si2F7. The tumor progression in mice was monitored using *in vivo* imaging to measure bioluminescence intensity for 21 days. Live imaging results (**Fig. 2-2 g**) and the quantitation of total bioluminescence intensity (BLI) calculated from the images (**Fig. 2-2**

h) indicated that mice injected with living 2F7-BR44 cells exhibited tumor growth. In contrast, none of the mice injected with vac-si2F7 developed tumors.

2.3.3 TLR agonist modification on the cryo-silicification of lymphoma prompts uptake and activation of dendritic cells.

Serving as antigen-presenting cells, dendritic cells (DCs) can initiate and regulate immune responses, building up an indispensable link between the innate and adaptive immunities. Different TLR agonists can activate different subsets of DCs and exert a synergistic effect on anti-tumor T cell responses. To evaluate the effect of TLR agonists, R848 and poly(I:C), we used propidium iodide (PI)-labeled 2F7-BR44 cells to prepare si2F7, si2F7-PEI, and vac-si2F7 and co-cultured them with human peripheral blood mononuclear cells (PBMCs) respectively. By monitoring the PI signals within DC subsets (CD11c⁺), we evaluated the uptake efficacy of samples by DCs. Compared to the no-treatment group, silica-coating, and PEI modification increased DC uptake efficacy from 1.7% to 9.4% and 10.6%, respectively. Further modified with poly(I:C) and R848, the vac-si2F7 induced a significant increase in DC uptake to 23% (**Fig. 2-3 a**). After sensing antigens from si2F7, si2F7-PEI, and vac-si2F7, DCs matured to initiate an immune response, identified as CD11c⁺CD80^{high} by flow cytometry. Both silica-coating and PEI modification promoted CD80 expression in CD11c⁺ subsets and thus enhanced DCs maturation compared to no treatment. Compared to 10% of CD80⁺ in control DCs, the CD80⁺ population increased ~2.5 fold with the treatment of si2F7 and si2F7-PEI. Moreover, the vac-si2F7 treatment resulted in 48.9% of CD80⁺ DC, illustrating its potency to promote DC maturation (**Fig. 2-3 b**). Based on endocytosis and DCs maturation, the vac-si2F7 group was selected for upcoming *in vitro* and *in vivo* studies.

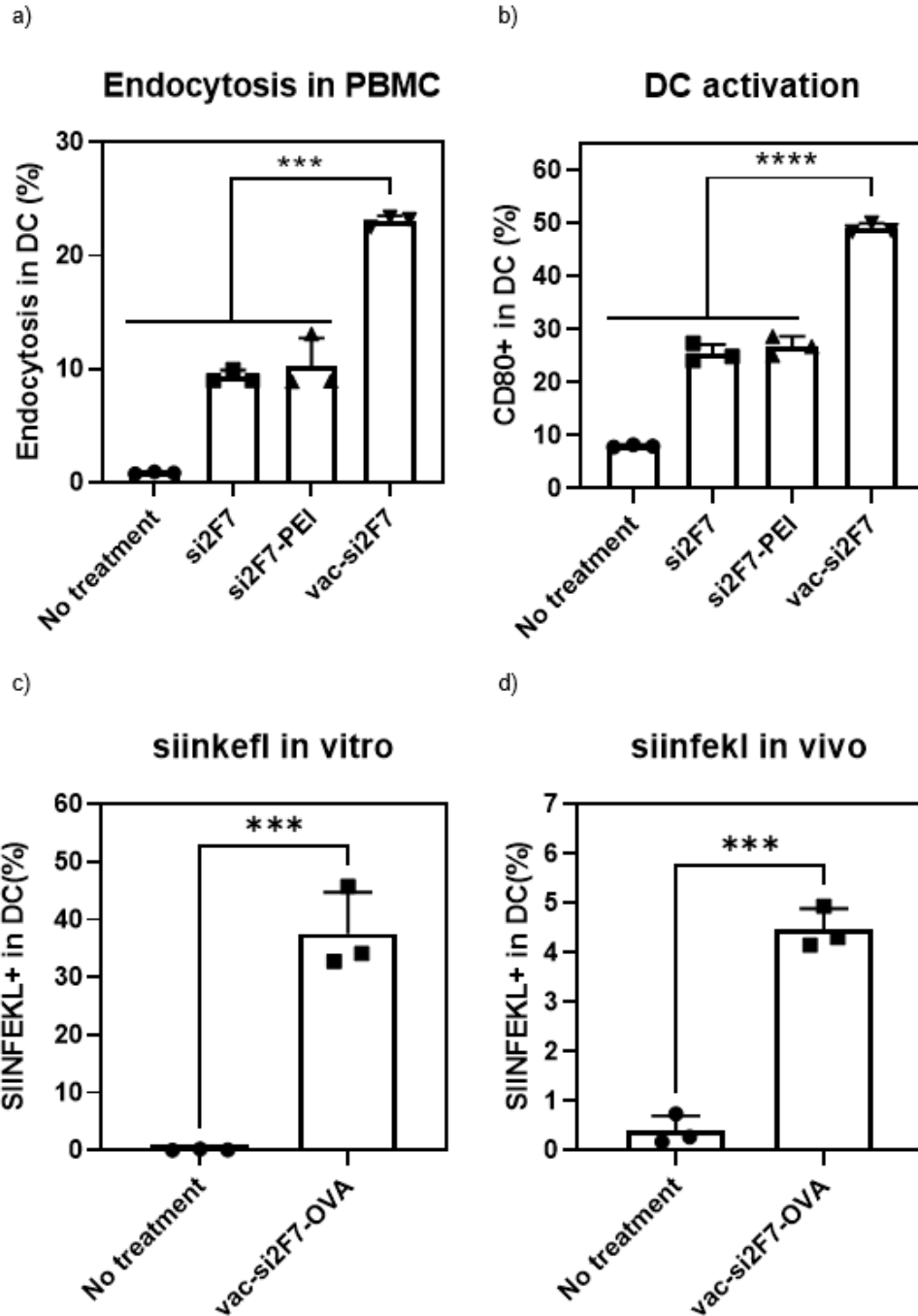


Fig. 2-3. Silicified cancer cells enhance the activation and induce a specific response of dendritic cells. **a**, Enhanced uptake of silicified cells with complete surface modification in dendritic cells (n=3 per group). **b**, percentage of activated dendritic cells measured by flow cytometry and representative dot plots of CD11c⁺ dendritic cells (n=3).

c, Percentage of OVA (SIINFEKL)-specific dendritic cells after incubating silicified cells with PBMC in vitro (n=3). **d**, Percentage of OVA (SIINFEKL)-specific dendritic cells in blood, 72 h after injecting silicified cells in mice (n=3). Data are presented as means \pm S.D. Statistical significance was calculated by t-test. ****P<0.0001, ***P<0.001.

Specific antigen presentation by DCs via the major histocompatibility complex class I (MHC I) is crucial for activating cytotoxic CD8⁺T cells (CTLs), alleviating concerns about systemic toxicity caused by the elevation of a broad immune response. Therefore, we first evaluated tumor-specific antigen presentation by DCs in an immunocompetent mouse model treated with cryo-silicified therapeutic vaccines. Due to the lack of standard antigen presentation from lymphoma, a model antigen—ovalbumin (OVA)—was genetically introduced into 2F7-BR44 cells using a lentiviral vector, creating 2F7-OVA cells. The cryo-silicified 2F7-OVA cells (vac-si2F7-OVA) were incubated with murine PBMCs from BALB/cJ mice. The immune response specific to OVA was evaluated by monitoring the expression of the SIINFEKL peptide epitopes on DCs after a 72-h incubation. Compared to untreated control, vac-si2F7-OVA showed a significant improvement of SIINFEKL presentation on DCs (**Fig. 2-3 c**). Tumor-specific antigen presentation by vac-si2F7-OVA was further investigated in BALB/cJ mice with their blood samples collected 3 days after IP injection of vac-si2F7-OVA. In accordance with the in vitro results, a significant increase in SIINFEK⁺ DCs was observed in peripheral blood of mice treated with vac-si2F7-OVA (**Fig. 2-3 d**). These results provide evidence that vac-si2F7-OVA can promote DC endocytosis, maturation, and specific antigen presentation.

2.3.4 The combination treatment of RTX and cryo-silicification of lymphoma inhibits lymphoma progression in xenograft humanized BLT mice.

Humanized BLT mice have been reported to support the reconstitution of human natural killer cells and macrophage in various tissues, including the brain⁸⁸⁻⁹⁰, providing an effective animal model for evaluating immunotherapy effectiveness. To assess the synergistic effect of vac-si2F7 and RTX, xenograft humanized NSG^{-Hc1}-BLT mice were established using 2F7-BR44 cells. The reconstitution of human immune cells in humanized NSG^{-Hc1}-BLT mice was tracked bi-weekly in peripheral blood starting 8 weeks post-BLT surgery (**Fig. 2-4**). Once the reconstitution levels stabilized, the humanized NSG^{-Hc1}-BLT mice were inoculated with 2F7-BR44 cells (1 million cells per mouse) through the tail vein and randomly separated into four groups for treatment with PBS, RTX, vac-si2F7, and a combination of RTX+vac-si2F7. The treatment details are summarized in **Fig. 2-5 a**. The RTX group received a single dose of RTX (12.5 mg/kg) via the tail vein injection 7 days post-xenograft. The vac-si2F7 group was intraperitoneally administered 4 doses of vac-si2F7, each containing 2 million si2F7, on days 7, 10, 21 and 24. Mice in the RTX+vac-2F7 group received the same RTX (12.5 mg/kg) on day 7, followed by the same vac-si2F7 regimen as the vac-si2F7 group. As a negative control, the PBS group was injected with PBS (100 μ l) through the tail vein on day 7, followed by additionally intraperitoneal doses of PBS (100 μ l) on days 7, 10, 21 and 24. Tumor progression was monitored for up to six weeks, with the condition that mice would be sacrificed early if their whole body bioluminescence from lymphoma reached 2×10^9 p/sec/cm²/sr (**Fig. 2-5 b**).

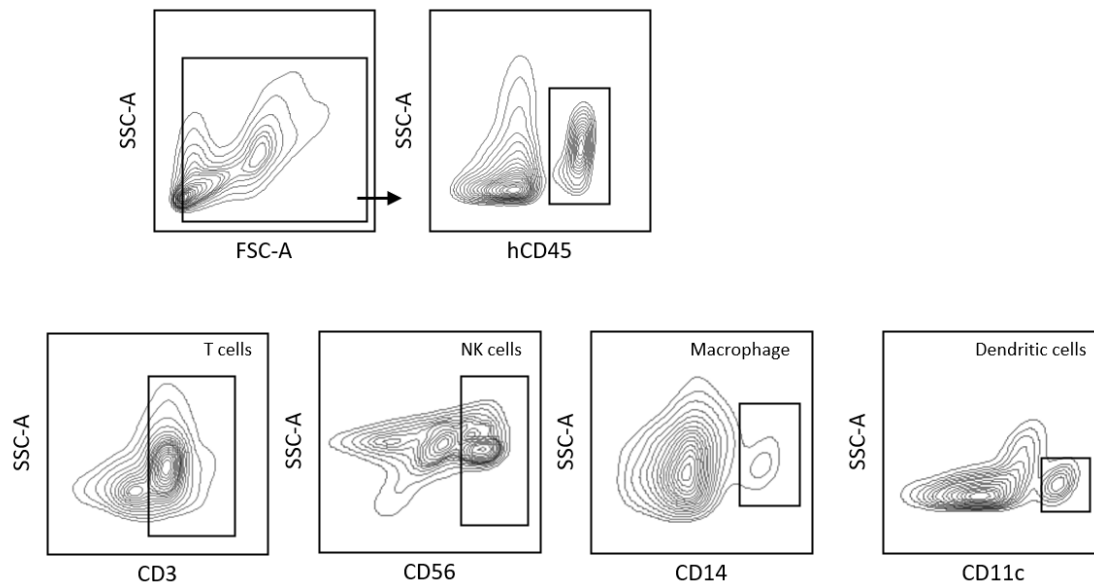


Fig. 2-4. Reconstitution of humanized BLT mice. Peripheral blood mononuclear cells were isolated from blood and stained with anti-human CD45, CD3, CD56 and CD14. Lymphocytes were first gated as CD45 positive population from singlets. T cells were gated as CD3 positive population under CD45⁺ population. Nature killer (NK) cells were gated as CD56 positive population under CD45⁺ population. Macrophage were gated as CD14 positive population under CD45⁺ population. Dendritic cells were gated as CD11c positive population under CD45⁺ population.

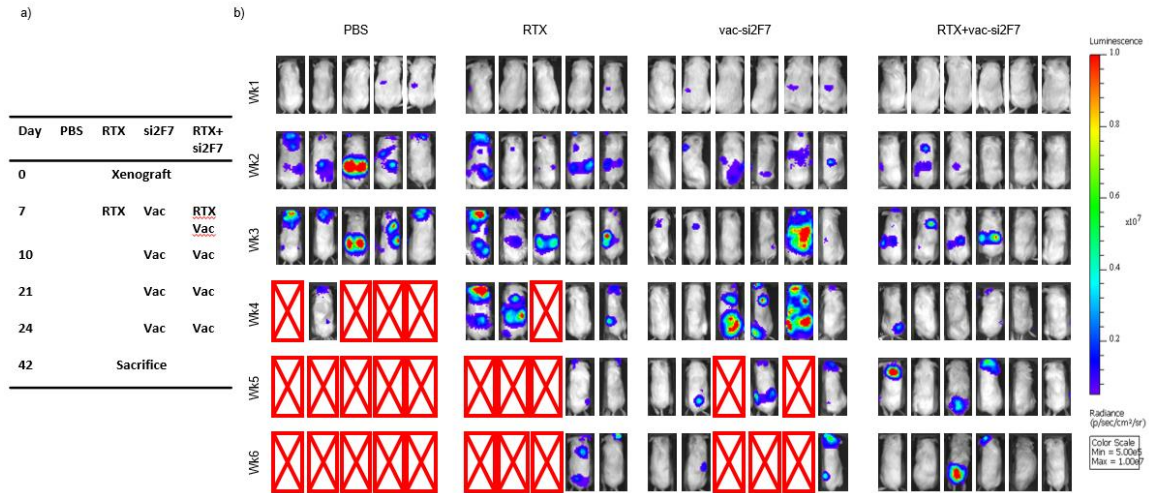


Fig. 2-5. Silicified cancer cells inhibit tumor growth in lymphoma xenograft humanized mice. a, Schematic of in vivo study design of silicified cells. **b,** In vivo imaging of tumor growth. Humanized BLT mice ($n=5$ to 6) inoculated with 1×10^6 2F7-BR44 lymphoma cells were treated with RTX (12.5 mg/kg) on Day 7 and 4 doses of silicified cells on Day 7, 10, 21 and 24.

We evaluated the survival rates using the Kaplan-Meier method across all groups. Compared to the PBS group, both RTX and vac-si2F7 treatments showed moderate inhibition of tumor growth. In contrast, the RTX+vac-si2F7 combination treatment significantly improved mouse life spans (**Fig. 2-6 a**). The treatment efficacy on the brain metastasis was dissected from the tumor burden in the body. While the PBS and RTX treatments exhibited comparable lymphoma progression, vac-si2F7 treatment initially reduced the tumor burden at week 3 but was ineffective by week 4. The combined RTX+vac-si2F7 treatment significantly inhibited tumor progression in both the brain (**Fig. 2-6 b**) and the rest of the body (**Fig. 2-6 c**). By the end of the study (day 42), tumor-bearing organs, including LNs (primary tumor sites) and metastatic sites like the brain and bone marrow, were collected following perfusion. Although NSG^{-Hc1} mice have only small

residual LNs, the 2F7-BR44 cells still metastasized to these LNs, resulting in the formation of large LN-like tumors^{91, 92}. As shown in **Fig. 2-6 d**, the RTX+vac-si2F7 exhibited the smallest LN sizes among all groups, indicating an effective suppression of tumor growth due to the synergistic effect of passive and adaptive immune responses. Moreover, compared to the other treatment groups, the RTX+vac-si2F7 combination was the most effective treatment in reducing tumor burden at both the primary (LNs) and metastatic sites (brain and BM), confirmed by lower mCherry expression from 2F7-BR44 cells within the total tissue cells (**Fig. 2-6 e, f, g**).

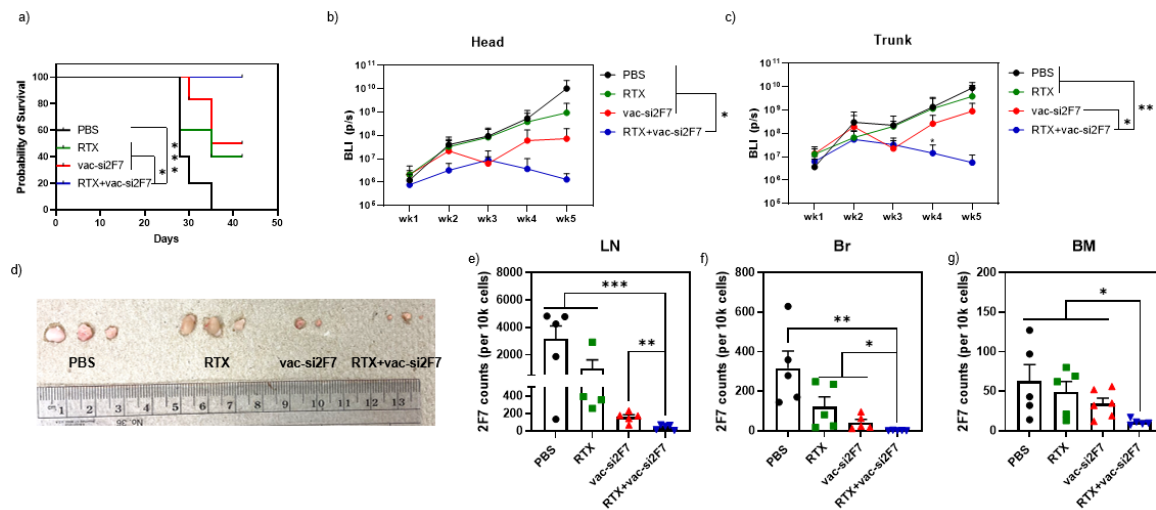


Fig. 2-6. Silicified cancer cells prolong survival and reduce tumor burden in lymphoma xenograft humanized mice. **a**, Kaplan-Meier survival curve of humanized mice. Statistical significance was determined by a two-way ANOVA test. **b-c**, BLI values in head area (**b**) and trunk area (**c**) were compared between mice treated with synergistic therapy and those treated with RTX alone. **d**, Representative Images of lymphoma lumps at lymphatic sites. **e-g**, Tumor burden in the lymph node (**e**), brain (**f**) and bone marrow (**g**) were shown in different groups. Statistical significance was determined by a two-tailed t-

test. Data are presented as means \pm S.E.M. Statistical significance was calculated by t-test. * $P < 0.05$, ** $P < 0.01$, *** $P < 0.001$. LN, lymph node. Br, brain. BM, bone marrow.

2.3.5 The combination treatment improves activation of effector cells and induction of memory cells in CD8⁺ T cells.

The ability of cryo-silicification of lymphoma to promote activation of effector T cells and induction of memory T cells was further investigated in spleens, peripheral blood, and bone marrow collected from the xenograft humanized BLT mice at the end time point (day 42). To examine the amplification of effector T cells and their tumor-specific activity in spleens, human CD3⁺ T cell percentages were evaluated in human CD45⁺ lymphocytes. As shown in **Fig. 2-7 a**, RTX+vac-si2F7 treatment had a significant increase in CD3⁺ T cells compared to other groups.

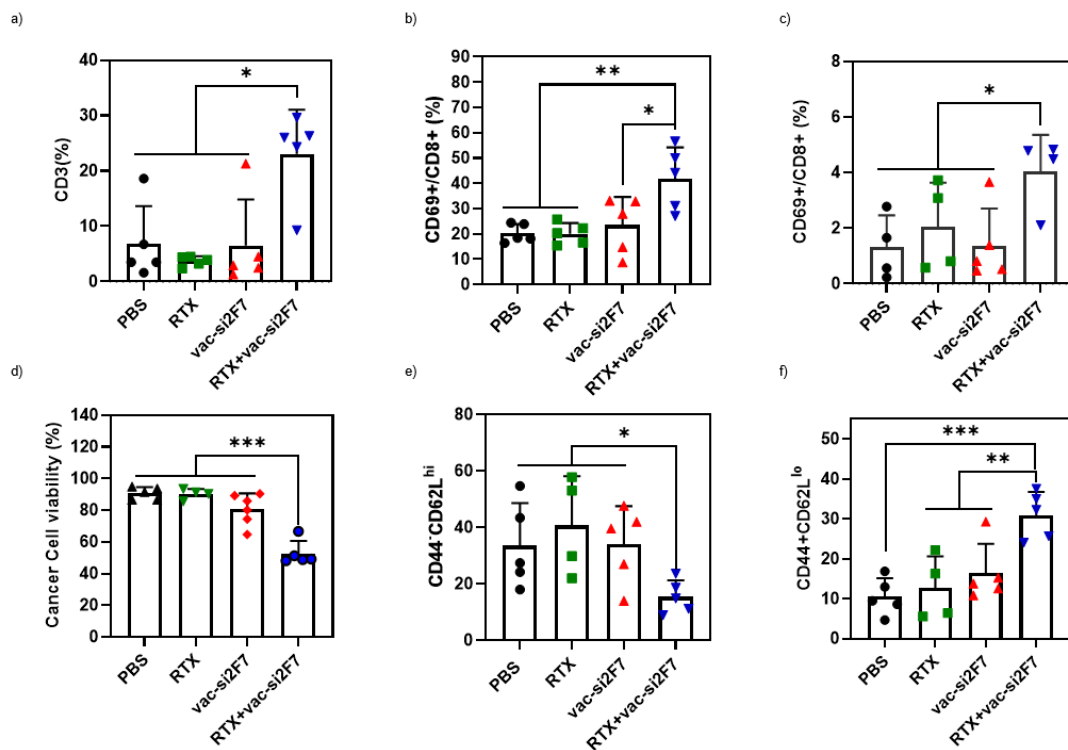


Fig. 2-7. Silicified cells activate 2F7-BR44 specific lymphocytes in spleen and train immune memory cells. **a**, Flow cytometry analysis of CD3⁺ T cell percentage in the spleen. **b, c**, Percentage of activated effector T cells in the blood (b) and bone marrow (c). **d**, 2F7-BR44 cell viability after incubation with effector T cells selected from the spleen. **e, f**, Silicified cells downregulate the percentage of naïve memory cells (e) and upregulate the percentage of effector memory cells (f) in vivo. Data are presented as means ± S.D. Statistical significance was determined by a two-tailed t-test. *P<0.05, **P<0.01, ***P<0.001

In addition, we evaluated the activation of CD8⁺ T cells in the blood and BM using CD69 expression, which is an essential step to fully functionalize effector T cells. The CD8⁺ T cells isolated from peripheral blood in mice treated with PBS and RTX showed comparable levels of CD69, while 3 out of 5 mice in the vac-si2F7 group exhibited a 1.5-fold increase. In accordance with the enhanced anti-tumor efficacy, mice treated with RTX+vac-si2F7 demonstrated a significant increase of CD69 expression by ~2-fold, compared to those of the other three groups (**Fig. 2-7 b**). Consistent results were obtained in CD8⁺ T cells isolated from BM, confirming the ability of RTX+vac-si2F7 treatment to enhance the activation of CD8⁺ T cells (**Fig. 2-7 c**).

Cytotoxic CD8⁺ T cells play a critical role in recognizing and eliminating cancer cells. To further assess the anti-tumor effectiveness induced by cryo-silicification of lymphoma, human CD8⁺ T cells were further enriched and evaluated for their specific cytotoxicity. Enriched CD8⁺ T cells were incubated with 2F7-BR44 cells and MT4 cells, an irrelevant human T cell leukemia cell line, served as a negative control, respectively. After 24h, cancer cell viability was calculated by monitoring the mCherry expression from

2F7-BR44 cells and EGFP expression in MT4 cells by flow cytometry. Due to the lack of exposure to the antigens from MT4 cells, CD8⁺ cells isolated from all groups showed minimal cytotoxicity (**Fig. 2-8**). However, CD8⁺ T cells isolated from both vac-si2F7 and RTX+vac-si2F7 demonstrated cell killing efficacy of 20% and 47% against 2F7-BR44 cells, respectively, compared to less than 10% cell death with cells from the treatment of PBS and RTX (**Fig. 2-7 d**), indicating the enhancement of tumor-specific T cell cytotoxicity induced by cryo-silicification of lymphoma.

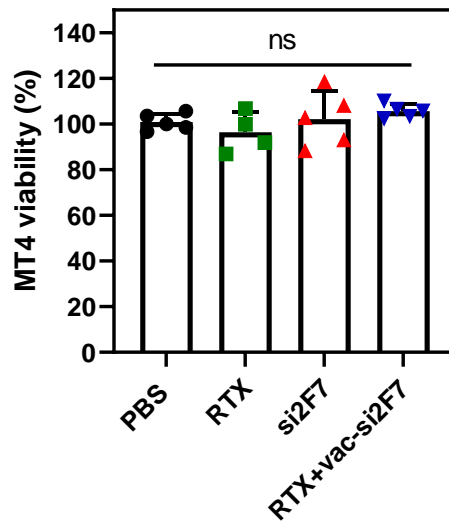


Fig. 2-8. Isolated effector T cells exhibited minimal cytotoxicity due to a lack of exposure. EGFP-transduced MT4 cells were incubated with 2F7-BR44 cells and effector T cells isolated from different groups. After overnight co-incubation, cells were measured with flow cytometry, and MT4 viability was calculated by comparing MT4 counts in each group with that in the group without adding effector T cells.

The induction of memory T cells plays a vital role to prevent cancer relapse, which is a unique advantage of therapeutic vaccination. Therefore, three major subsets of CD8⁺ T cells were further defined by CD44 and CD62L (L-selectin) surface markers: naïve (CD44^{low}CD62L^{high}), central memory (CD44^{high}CD62L^{high}), pre-effector-like (CD44^{low}CD62L^{low}), and effector/memory (CD44^{high}CD62L^{lo}). In the RTX+vac-si2F7 group, there was a reduced count of naïve memory cells, showing a CD44-CD62L^{high} ratio of 15.5% (**Fig. 2-7 e**). This contrasts with the PBS group at 33.5%, the RTX group at 40.7%, and the group receiving only vac-si2F7 at 35.6%. In addition, an elevated level of effector memory cells at 30.9% was observed in the RTX+vac-si2F7 treated mice, compared to 10.6%, 11.6%, and 16.4% in the PBS, RTX, vac-si2F7 groups, respectively (**Fig. 2-7 f**). These experiments revealed that the RTX+vac-si2F7 treatment generated superior cytotoxicity of T cells and enhanced the effector memory T cell population.

2.3.6 The combination treatment provides specific protection from tumor growth.

To ensure the observed therapeutic outcomes of the combination treatment were not a result of non-specific immune responses triggered by HLA mismatch, we developed a control vaccine (vac-siCtrl) using an unrelated tumor cell line, MB-MDA-231, a human-derived breast cancer cell line. Humanized BLT mice were inoculated with 2F7-BR44 cells (1 million cells per mouse) and randomly separated into 3 groups at week 8 post-BLT surgery. In the RTX group, mice were treated with native RTX (12.5 mg/kg) via tail vein on days 7 post xenograft. Mice in both combination treatments were first treated with native RTX (12.5 mg/kg) on day 7, followed by 4 doses of vac-si2F7 or vac-siCtrl on day 7, 10, 21 and 24 in RTX+vac-si2F7 or RTX+vac-siCtrl groups, respectively (**Fig. 2-9 a**). Tumor progression was weekly monitored by *in vivo* bioluminescence imaging (**Fig. 2-9 b**). The

treatment of RTX+vac-siCtrl showed no synergistic effect but had comparable therapeutic efficacy to RTX alone treatment: only 20-40% of mice formed lymphoma in the body area under treatment, however, 80-100% of mice developed CNS metastasis. In contrast, no obvious bioluminescent signals were found in all mice treated with RTX+vac-si2F7 by week 4.

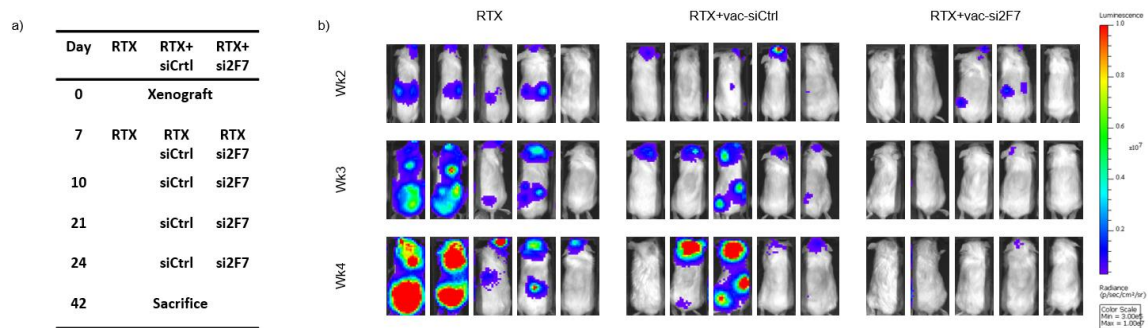


Fig. 2-9. Silicified cells induce specific anti-lymphoma responses towards wrapped cancer cells. **a**, Schematic of in vivo study design. Humanized mice (n=5) were injected with 2F7-BR44 cells (1×10^6 cells per mouse) on Day 0 via the tail vein. Mice then were randomly separated into 3 groups for treatment on Day 7, 10, 21 and 24. Tumor progression was monitored with IVIS weekly. Mice were re-challenged with 2F7-BR44 cells (1×10^6 cells per mouse) on Day 28. **b**, Tumor bioluminescent signal biodistribution in humanized BLT mice.

To further compare the specific cytotoxicity of T cells, $CD8^+$ T cells were isolated from spleen after the second tumor challenge, and their cytotoxicity was evaluated in co-incubation with equal cell numbers of targeting cells (2F7-BR44 cells) and control cells (MT4 cells) at the E:T ratio of 1:2. The $CD8^+$ T cell cytotoxicity was calculated using the reporter protein mCherry and EGFP in 2F7-BR44 cells and MT4 cells by flow cytometry, respectively. Isolated effector T cells exhibited limited cytotoxicity to control cells (MT4

cells) due to a mismatch of vaccination antigens and MT4 cell surface proteins (**Fig. 2-10**). Compared to the Ctrl (no CD8⁺ cells), effector CD8⁺ T cells trained by vac-siCtrl cells lacked the ability to induce cytotoxicity in 2F7-BR44 targeting cells. However, CD8⁺ T cells from the RTX+vac-si2F7 group induced a significant decrease of targeting cell viability, demonstrating specific T cell immunogenicity induced by the combination treatment (**Fig. 2-11**).

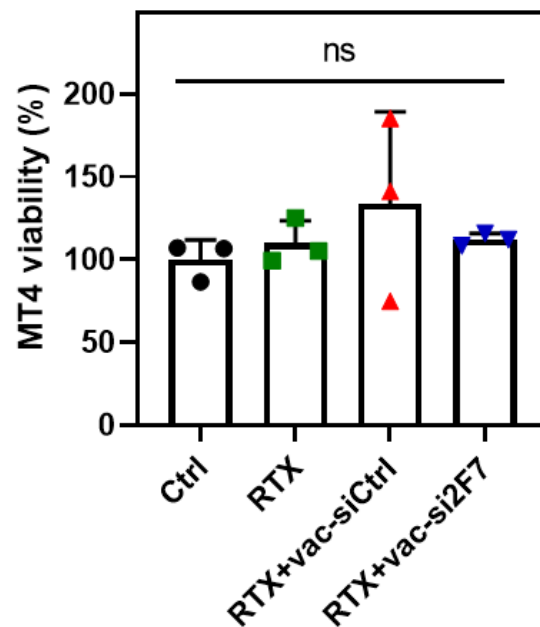


Fig. 2-10. Isolated effector T cells exhibited minimal cytotoxicity due to a lack of exposure after the second challenge. EGFP-transduced MT4 cells were incubated with 2F7-BR44 cells and effector T cells isolated from different groups. After overnight co-incubation, cells were measured with flow cytometry, and MT4 viability was calculated by comparing MT4 counts in each group with that in the control group.

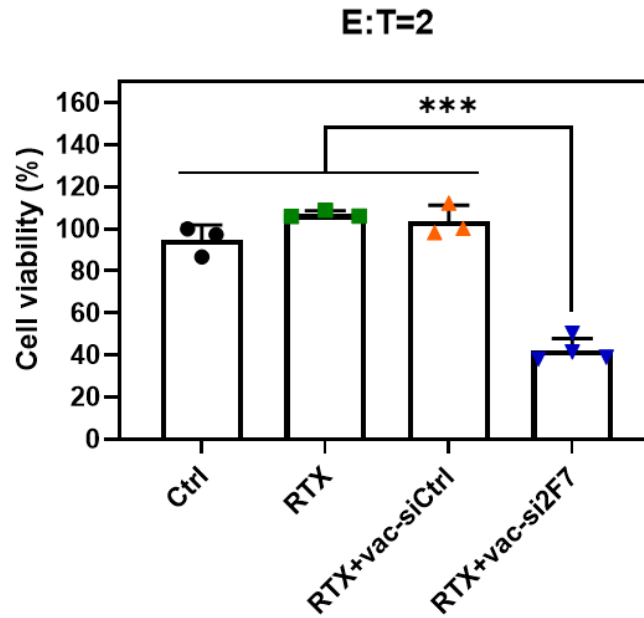


Fig. 2-11. 2F7-BR44 cell viability after incubation with effector T cells selected from the spleen. Data are presented as means \pm S.D. Statistical significance was determined by a two-tailed t-test. ***P<0.001.

2.3.7 The combination treatment prevents tumor relapse.

Encouraged by the efficacy of the combination treatment in inhibiting tumor progression and CNS metastasis, we evaluated the improvement of the combination treatment for preventing tumor progression and relapse by inducing the immune memory effect. The long-term protection was further tested in the treated mice with a tumor burden lower than 3×10^8 total photons by week 4. Three out of five mice in the RTX and RTX+vac-siCtrl groups and all five mice in the RTX+vac-si2F7 group were proceeded with a rechallenge of 2F7-BR44 cells on day 28 and successively monitored for 3 weeks. All mice showed delayed tumor progression, indicating a possible anti-tumor memory response. However, mice in the RTX and RTX+vac-siCtrl groups showed tumor

progression in original sites or new formation, resulting in low survival rates due to insufficient immune memory induced by RTX alone. In contrast, the combination treatment successfully inhibited tumor growth (**Fig. 2-12**) by reducing tumor burden in both primary sites (lymph nodes, **Fig. 2-13 a**) and metastatic sites (brain, **Fig. 2-13 b**).

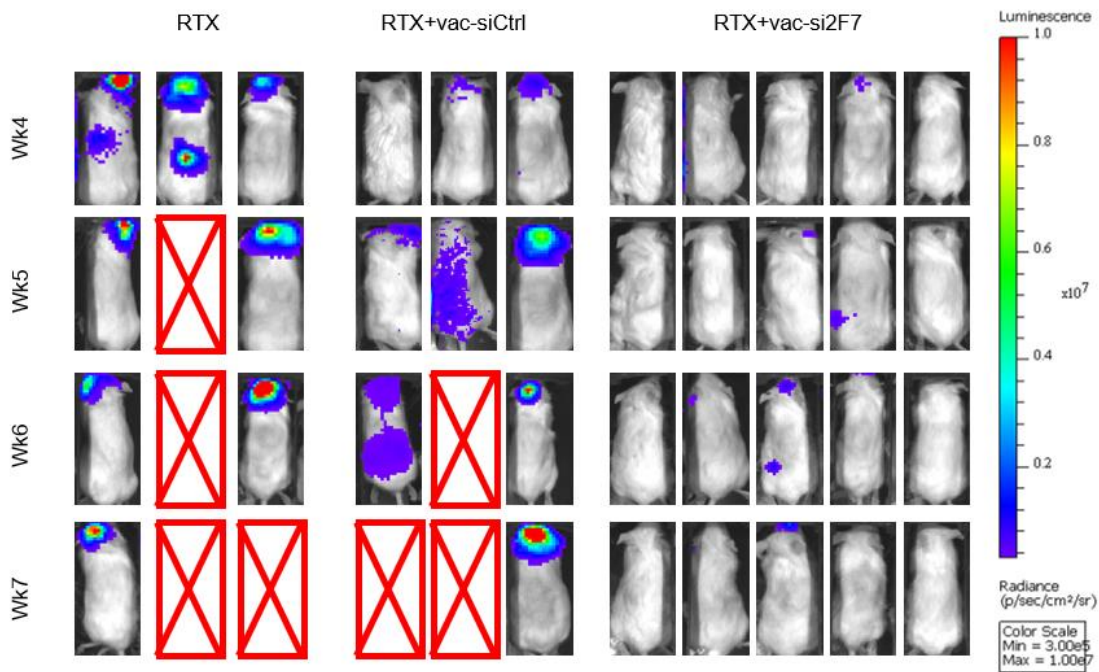


Fig. 2-12. Tumor progression after re-challenged with 2F7-BR44 cells. The long-term protection was further tested in the treated mice with a tumor burden lower than 3×10^8 total photons by week 4. Mice were re-challenged with 2F7-BR44 cells (1×10^6 cells per mouse) on Day 28. Tumor progression was monitored with IVIS weekly.

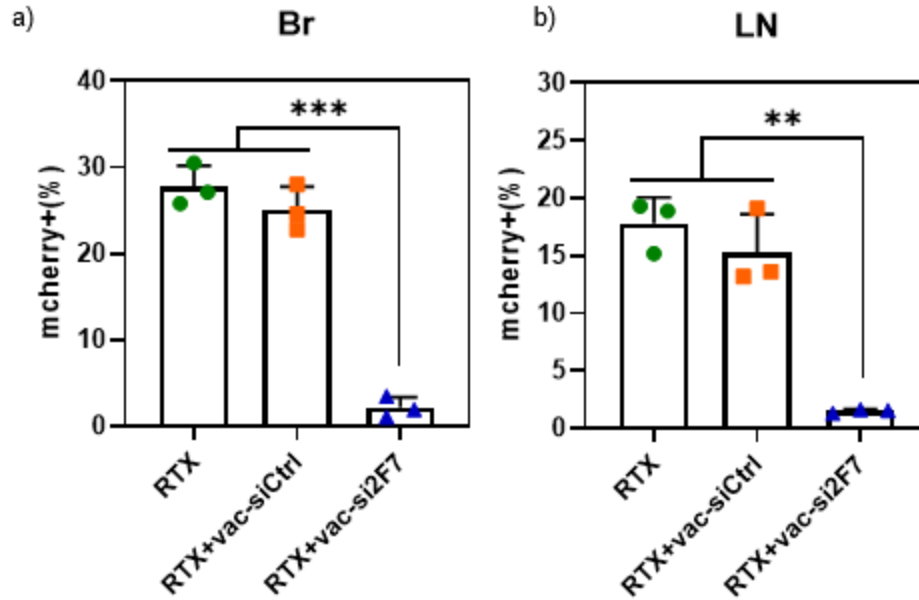


Fig. 2-13. Tumor load of 2F7-BR44 cells in brain (a) and lymph node (b).

The tumor clearance in the metastatic site was also confirmed in kidneys by hematoxylin and eosin (H&E) staining. As shown in **Fig. 2-14**, clear tumor nests (dark sections) were found in the kidney tissue slides from both RTX and RTX+vac-siCtrl groups, while no obvious tumor was shown in kidney slides from the RTX+vac-si2F7 group. These results demonstrate that synergistic therapy generates specific immune memory to inhibit potential tumor relapse.

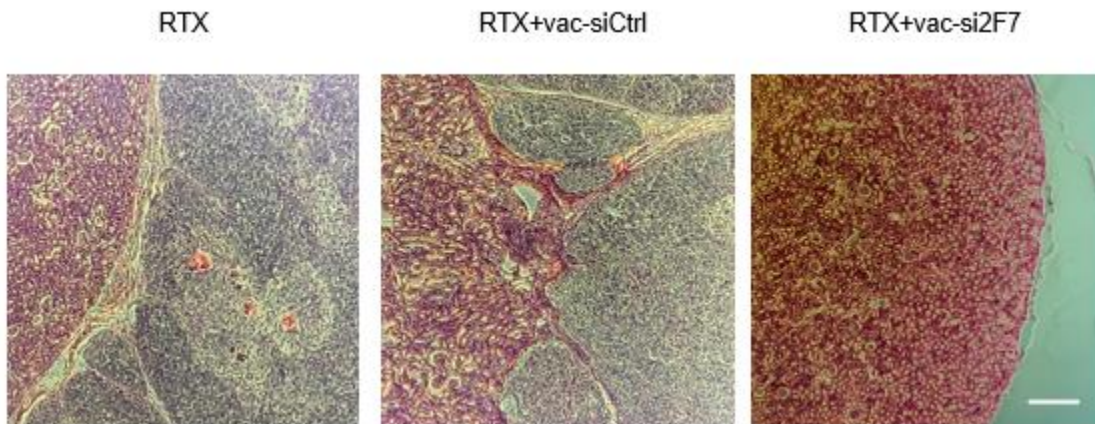


Fig. 2-14. H&E staining of kidney (Scale bar: 200 mm).

2.3.8 The combination treatment exhibits a biosafety profile.

RTX has been widely used in clinics without safety concerns. Thus, the biosafety analysis of combination treatments, including RTX+vac-siCtrl and RTX+vac-si2F7, was compared to RTX treatment, ensuring that the therapeutic vaccines impart no extra toxicity to RTX. To address the concerns on possible inflammation induced by the therapeutic vaccine, the heart, liver, lung, and brain were collected and subjected to H&E staining. As shown in **Fig. 2-15 a**, no morphological changes or tissue damage were observed in combination treatment groups. Furthermore, systemic biosafety was monitored by measuring the levels of the aspartate transaminase (AST) and alanine transaminase (ALT) to assess liver toxicity, as well as uric acid and albumin in blood stream as renal function tests. All the readouts for the combination groups were comparable to those of the RTX group and remained within the normal ranges (**Fig. 2-15 b,c**). Collectively, these findings revealed the absence of significant systemic toxicity in mice treated with the combination treatment, underscoring its biocompatibility and biosafety for possible translational applications.

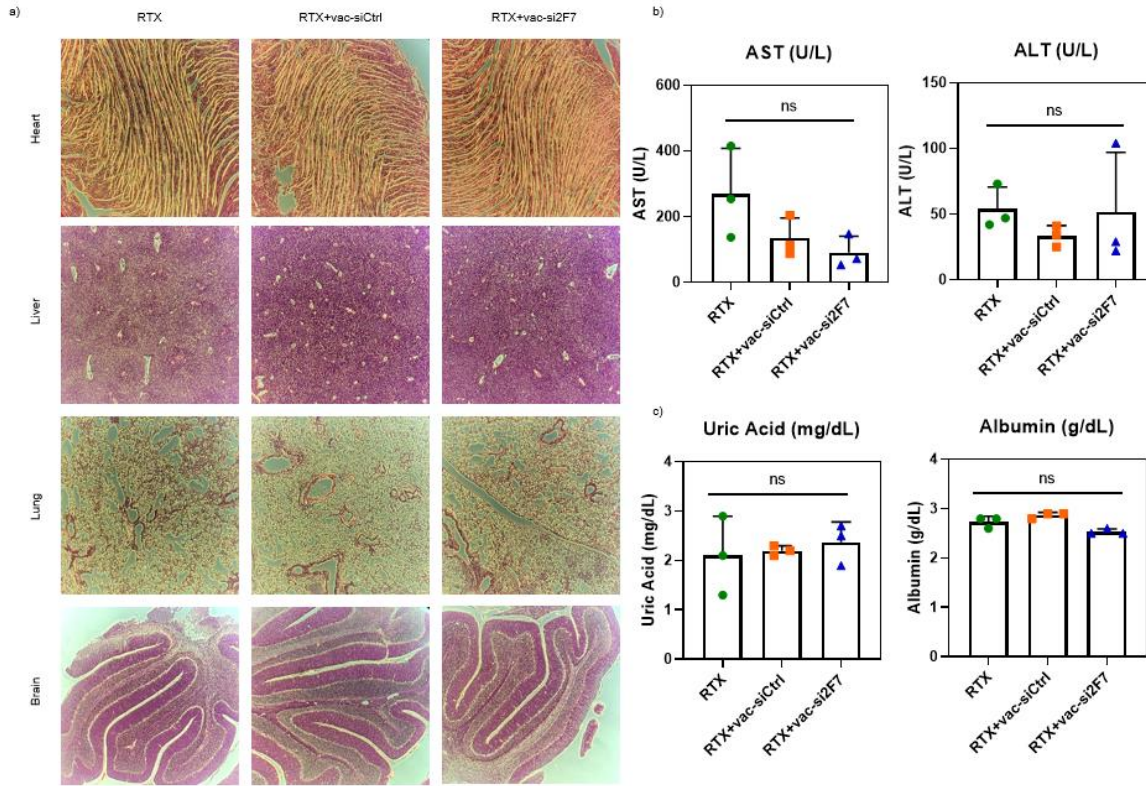


Fig. 2-15. Evaluation of systemic toxicity. **a**, Pathology analyses of major organ sections from humanized mice by H&E staining. **b-c**, Hepatic (b) and renal (c) function assessment of humanized mice (n=3). Data are presented as means \pm S.D. Statistical significance was calculated by t-test. ns, no significance. AST, Aspartate transaminase. ALT, Alanine transaminase.

2.4 Conclusion and discussion.

We developed a synergistic therapy of whole-cell based tumor vaccine and FDA-approved monoclonal antibody, with the generation of immediate protection and specific tumor immune response. This resulted in an outstanding therapeutic outcome in primary and metastatic tumors and inhibition of potential tumor relapse, which merged the advantages of passive and active immunity, as expected. Cryo-silicification technology

preserved intact tumor cell structure and antigens on the surface, resulting in effective and comprehensive presentation efficacy to dendritic cells. The silica framework also enabled surface modification such as with toll-like receptor agonists, which promoted endocytosis and activation of dendritic cells. Silicified vaccine cells also generated alleviated expression of specific antigens of MHC I both in vitro and in vivo, providing the evidence of specific protection upon primary and relapsed tumor.

To translate our developments to cancer patients, we utilized a humanized mice model, which is usually used to mimic the human immune system to evaluate the efficacy and safety of therapeutics before moving to human clinical trial. Reconstitution of lymphocytes and the complement system enabled a broader cell death mechanism in humanized mice. What's more, both the cell strain wrapped in the tumor vaccine and the clinical strategy are substitutable, signifying a feasible path in the future in establishing a comprehensive platform capable of accommodating a diverse frame of tumor models.

Although monoclonal antibody therapy is widely used as a first-line medication in anti-tumor treatment strategies, potential limitations exist due to its limited half-life and tumor heterogeneity. Here, we designed the silicified cancer cell as a therapeutic vaccine, which possesses two advantages—immediate cancer eradication and sustained defense, by activating T cells and establishing a durable immune memory. A key feature of our strategy is its adaptability; the encapsulated cell strains can be customized, providing a potential platform for personalized treatment to meet individual patient needs.

Rituximab is commonly used as a first-line treatment for several types of non-Hodgkin lymphoma but faces critical obstacles: (1) Its efficacy in rapidly eradicating lymphoma cells is limited, and it induces the loss of CD20 expression on lymphoma cells,

facilitating tumor evasion; (2) Despite Rituximab-induced cytotoxicity eliciting an immune response, this is insufficient for generating adequate effector cells and durable immune memory (**Fig. 2-1**). Synergistic administration with chemotherapy increases the concern of adverse effects on healthy tissues. Thus, we propose an adjunctive approach combining Rituximab with a therapeutic vaccine, cryo-silicified whole lymphoma cells, preserving cellular structure without viability (**Fig. 2-2**).

When introducing therapeutic vaccines to regulate the immune response, vaccines must be processed and presented by dendritic cells in three steps. (1) Therapeutic vaccines are uptaken by immature dendritic cells (iDCs, **Fig. 2-3 a**). (2) Upon detection of antigens, the iDCs transition into a mature state, becoming fully functional and capable of initiating an immune response (**Fig. 2-3 b**). (3) Dendritic cells express antigenic peptides in association with MHC molecules classes I and II (**Fig. 2-3 c-d**) and further contact with T cells to activate immune system (**Fig. 2-7**).

To translate our developments to cancer patients, we utilized a humanized mice model, which is usually used to mimic the human immune system to evaluate the efficacy and safety of therapeutics before moving to human clinical trial. While it doesn't replicate the entire human immune system, it enables a wide array of cell death mechanisms by providing a complement system and necessary lymphocytes, including T cells, nature killer cells and dendritic cells (**Fig. 2-4**). Within the BLT-humanized mice model, synergetic therapy sufficiently inhibits the primary lymphoma (**Fig. 2-5. Fig. 2-6**), prevents potential tumor relapse (**Fig. 2-12**) with a biosafety profile (**Fig. 2-15**).

Chapter 3: Advancing Monoclonal Antibody Therapy with Targeted Delivery to Lymph Nodes.

3.1 Introduction.

3.1.1 Metastatic pathway and physiology of lymphatic system.

Metastasis involves the spread of cancer cells from the primary tumor to surrounding tissue or to distant organs. It's the primary cause of cancer morbidity and mortality⁹³⁻⁹⁵ which is estimated to be responsible for 90% of cancer deaths⁹⁶. Tumor growths are classified into a four-stage progression framework. Stage I is characterized by confined neoplastic cells within the primary anatomical boundary, referred to as localized cancer. Stage II and Stage III are collectively termed as regional cancer, delineating the initiation of malignant cell migration to proximate lymphatic structures, albeit without invasion into distal organ systems. Stage IV is designated for cases where distant metastatic dissemination is evident, indicative of the malignant cells establishing secondary neoplastic sites beyond the regional boundaries. When cancer is detected at an early stage or before metastasis, traditional treatment strategies, including surgery and local irradiation have a successful treatment outcome and the patients have a better possibility of being cured. Once the tumor is detected after metastasis, treatments are less successful, and the 5-year survival rate is reduced as a result in various types of cancer (**Table 3.1**). Additionally, many patients may not present with a detectable metastasis at the point of initial diagnosis, however, subsequent assessments will find the metastases at a later time. Metastases in certain organs, such as metastases to central nervous systems and bone

marrow, might occur years or even decades after the successful treatment of the primary tumor⁹⁷.

Table. 1. Five-year survival percentage in different stages of cancer⁹⁴.

Site	Localized Phase 1	Regional Phase II-III	Distant Phase IV	Unknown
Intestine	89.8%	71.1%	13.8%	35.0%
Kidney	92.6%	68.7%	11.6%	38.0%
Lung	80.0%	56.5%	25.0%	5.6%
Melanoma	98.4%	63.6%	22.5%	83.7%
Ovary	92.4%	75.2%	29.2%	24.3%
Uterine	94.9%	68.6%	16.3%	52.0%

The metastatic process consists of a series of steps. Before metastasis, angiogenesis occurs to meet the need for blood supply for tumor progression and to provide a potential escape route⁹⁸. Angiogenesis, the process of forming new blood vessels from pre-existing ones, is a complex biological process regulated by a balance between pro-angiogenic and anti-angiogenic factors, with the help of cytokines and chemokines such as vascular endothelial growth factor (VEGF), fibroblast growth factors (FGFs) transforming growth transfer beta (TGF- β), interleukins (ILs), C-X-C motif chemokine ligand 12 (CXCL12) and tumor necrosis factor alpha (TNF- α)^{99, 100}. These factors can be secreted directly by the tumor cells or by stromal cells, such as macrophages or monocytes and they attract tumor cells to lymphatic vessels^{101, 102}. The presence of tumor cell has been implicated in the induction of lymphangiogenesis within the lymph nodes, characterized by the

proliferation of additional lymphatics in the nodes^{103, 104}. It can also change the morphology and function of various vessel types in the lymph nodes, providing potential sites for rearrangement of the vessel structures or abnormal connections between vascular and lymphatic networks^{105, 106}.

The metastatic process in oncology encompasses multiple mechanisms, among which are direct invasion of adjacent tissues, hematogenous dissemination, and lymphatic spread. Tumoral cells that exhibit a high degree of aggressiveness may infiltrate nearby stromal tissue, a process termed as direct cancer invasion. This method of extension is less frequently observed in clinical scenarios.

Blood vessels provide oxygen and nutrients to growing tumor cells, which may outgrow their blood supply and become hypoxic. Hypoxia stimulates the over-expression of a few genes, including Vascular endothelial growth factor (VEGF). The new blood vessels may break, allowing cancer cells to invade the bloodstream. Once cancer cells enter the bloodstream, many of them will die from stresses associated with circulatory passage. Only the cells which can resist death, may attach to capillaries through adhesion receptors, and then form a metastasis. Despite this attractive hypothesis, there is no evidence or direct observation of invasion of intra- or peritumoral blood vessels. Most tumors metastasize to sentinel lymph nodes first and then may enter blood stream via the blood fluid circulation. The circulating tumor cells in blood have been widely investigated, for early diagnosis, prognostic evaluation and prediction of recurrence or therapeutic efficacy. FDA has approved several methods for CTCs detection in blood.

Conversely, in the lymphatic spread pathway, malignant cells infiltrate the lymphatic system and secrete growth factors and chemokines that may augment the

diameter of lymphatic vessels, thereby facilitating metastatic spread. Furthermore, malignant cells can traverse from lymph nodes to distant organs by entering the bloodstream via vessels connected to the lymphatic system or through major lymphatic ducts such as the thoracic duct, culminating in systemic dissemination. Both clinical data and animal model studies substantiate that, for the majority of cancers, lymphatic vessel-mediated spread is the predominant route of metastasis¹⁰⁷⁻¹¹⁰. Given that in many cases the primary tumor is surgically excised or treated with monoclonal antibody, undetectable cancer cells populations hiding in lymph nodes still engage the possibility of outgrowing to clinically diagnosable metastasis after many years, bringing the risk of tumor relapse^{111, 112}. Eliminating tumor cells in lymph nodes could be helpful to restrict tumor spread from remnant cells and potential tumor relapse¹¹³.

Lymph nodes function as specialized biological structures, located across the human body. Besides being central hubs for tumor metastasis, lymph nodes also work as central hubs for the initiation and regulation of adaptive immune responses¹¹⁴. These lymphoid tissues provide an environment where immune cells, primarily leukocytes, are summoned from the bloodstream¹¹⁵. These immune cells engage in the critical task of examining antigen-bearing lymph fluid, which is systematically transported from body tissues. This screening process facilitates the identification and subsequent response to foreign pathogens, playing a vital role in body defensive mechanisms. Consequently, the efficacy of vaccines is intrinsically linked to the operational integrity of lymph nodes. Vaccines leverage the immunological functions of lymph nodes, to elicit a robust and targeted immune response, making these structures indispensable for the desired immunogenic effects of vaccination^{116, 117}. United States Food and Drug Administration

approved Gardasil® and Cervarix® vaccines work against human papillomavirus infections, which are linked to cervical cancer, consisting of virus-like protein nanoparticles and enhancing access to lymph nodes compared to viral antigens¹¹⁸. What's more, Pfizer's COVID-19 vaccine has been shown to allow robust immune protection, by inducing persistent germinal center B cell response in the axillary lymph node^{119, 120}.

The lymphatic vasculature serves as a critical unidirectional conduit facilitating the movement of fluids, solutes, and cellular constituents from peripheral tissues to lymph nodes¹²¹. This system begins with blind-ended initial lymphatic capillaries, which are uniquely composed of loosely overlapping lymphatic endothelial cells (LECs)¹²². These cells exhibit incomplete intercellular junctions, strategically enabling the transcapillary migration of interstitial fluids. This process is dynamically modulated by mechanical forces such as skeletal muscle motion and is crucial for effective lymph drainage^{123, 124}.

At the architectural core of the lymphatic system are the lymph nodes, structured to orchestrate the precise and timely interactions among antigens, antigen-presenting cells (APCs), and lymphocytes¹²⁵. This intricate structure not only facilitates immune surveillance and response but also critically influences the distribution of malignant cells, pathogens, or nanoparticles within the nodes upon their entry via the lymphatic stream. Lymph enters the lymph nodes through the afferent lymphatic vessels, arriving first at the subcapsular sinus (SCS)^{126, 127}. The SCS is characterized by a specialized luminal architecture, delineated by a monolayer of LECs interspersed with strategically positioned lymph-sampling macrophages and dendritic cells. This cellular arrangement forms a selective barrier, controlling lymph access to the deeper lymph node parenchyma and thereby directing the dispersion of lymph predominantly along sinus pathways. From the

SCS, lymph progresses through a network of interconnected sinuses—namely the medullary, transverse, and cortical sinuses, all lined with LECs—before exiting the lymph node via efferent lymphatic vessels. However, a conduit system composed of fibroblastic reticular cells allows a portion of lymph and solutes deeper access to the lymph node parenchyma, where the majority of resident leukocytes reside^{128, 129}. This conduit system delivers lymph and low molecular weight solutes to the lumen of specialized vascular structures of the lymph node, known as the high endothelial venules (HEVs).

High endothelial venules (HEVs) are specialized blood vessels, present in all secondary lymphoid organs with the exception of the spleen, and include hundreds of lymph nodes all around the body¹³⁰. From the cortical-paracortical junction to the paracortex of lymph nodes, HEVs exhibit a progressive increase in size¹³¹. HEVs are uniquely identified by the expression of peripheral node addressin (PNAd), a ligand for L-selectin, distinguishing HEVs from other blood vessels both within and beyond lymphoid organs. MECA-79 is an antibody that specifically identifies 6-sulpho sialyl Lewis^x, a functional carbohydrate epitope on PNAd that binds L-selectin¹³². As such, MECA-79 serves as a widely used marker for detecting PNAd.

The process by which lymphoma cells home back to lymph node involves the adhesion molecules expressed on lymphoma cells engaging with certain ligands on the lymphatic system, mimicking the homing mechanism used by normal lymphocytes^{131, 133}. For diffuse large B cell lymphoma (DLBCL), a type of non-Hodgkin lymphoma, the lymphoma cells express L-selectin as the adhesion molecule. Corresponding ligand is PNAd expressed on HEVs^{134, 135}. In this case, MECA-79 inhibits DLBCL cells homing back to lymph nodes by competitive inhibition¹³⁶. Thus, MECA-79 is a promising ligand

for guiding nanoparticles to specifically gather in lymph nodes, while also helping to obstruct lymphoma cells from homing back to lymph nodes, contributing to a reduction in metastasis.

3.1.2 Current art of lymph-node targeting nanoparticles.

Given that the design and application of lymph-node targeting represent a significant advancement in vaccine efficacy and cancer treatment, several lymph-node targeting delivery platforms have been developed and reported. Intranodal injection provides the most direct and efficient delivery strategy to the lymph node, which usually requires surgery¹³⁷, ultrasound guidance¹³⁸ or tracer dyes¹³⁹. Intranodal injection was first used for lymphangiography by directly injecting an oil-based contrast agent into inguinal lymph nodes¹⁴⁰. As it developed, antigen-loaded dendritic cells were intranodally injected into eighteen patients with clinical renal cell carcinoma. Among the eighteen patients, nine patients showed tumor reduction, including three with complete response (CR)¹⁴¹. In another report of twenty-six patients with metastatic colorectal cancer, a vaccine administered via intranodal injection induce tumor-antigen-specific T-cell responses in more than 60% of the patients. It also enhanced clinical outcomes, extending the recurrence-free survival rate to a duration of 5 years¹⁴². However, intranodal injection is complex and has the potential risk. In addition, lymph nodes are small, limiting the injection volume.

Interstitial injection promotes the entry of nanocarriers into lymphatic capillaries, and after that, vehicles drain from the capillaries into lymph nodes. Interstitial injection includes subcutaneous, intramuscular, and intradermal injection. Given that the size of nanocarriers influences the efficacy to enter the interstitial fluid and consequently the

lymph nodes, only vehicles smaller than 10 nm can enter vascular capillaries^{143, 144}. On the other hand, nanocarriers cannot be too small. Although small carriers enter into vascular or lymphatic capillaries easily, they are quickly cleared away because their flow rate is over 100-fold higher through vascular capillaries than lymph capillaries. In addition to size, surface charge also affects lymph-node targeting efficacy. The Interstitium is mainly composed of collagen fibers and glycosaminoglycans, which are negatively charged¹⁴⁵. As a result, cationic nanocarriers tend to be trapped in the extracellular matrix, while neutral or negative charge promotes the transfer efficacy of nanocarriers¹⁴⁶. Modifying the nanocarriers with albumin, dextrans and histamine also promotes lymphatic uptake efficacy, which can increase the interstitial oncotic pressure and have the preference to be uptake by lymphocytes^{147, 148}.

However, the current approach to target lymph nodes, by administering small molecule cargoes through peripheral routes, faces risk of tissue damage and uneven distribution. Given that monoclonal antibody therapy is on a rise as therapeutics with more than 100 products approved by the FDA¹⁴⁹, a systemic administered protein delivery cargo with the capacity of lymph-node targeting is necessary.

3.1.3 Nanoencapsulation platform for enhanced efficacy of protein therapeutics.

The protein nanocapsule technology has been innovatively developed by our group, whereby an individual protein is encapsulated by a polymer shell formed *via in situ* polymerization of monomers and crosslinkers¹⁵⁰. The nanocapsules have successfully encapsulated various proteins¹⁵¹, also including enzymes¹⁵² and monoclonal antibodies⁷⁶, exhibiting improved stability and prolonged circulation time. By adjusting monomers and crosslinkers, nanocapsules can release cargo under control and bypass the blood-brain

barrier (BBB). Functional groups can be introduced on the surface of nanocapsules to enable further modification and targeted accumulation at specified sites¹⁵⁰. Briefly, polymerizable vinyl groups are first covalently linked to the protein. Subsequent polymerization in an aqueous solution containing monomers and crosslinkers wraps each protein core in a polymer shell. After encapsulation, TEM and DLS analysis show that the size of protein nanocapsules is around 30 nm. The stability and activity of the nanocapsules have also been proved *in vitro* and *in vivo* using a confocal fluorescent imaging system and an MTT assay.

However, the modification of vinyl groups on the protein surface may influence the protein structure and induce incomplete release of protein cores, existing a potential risk of hampering protein activity in further experiments. To address this limitation, nanocapsules encapsulating unmodified proteins through non-covalent bonds have been developed. By adjusting the pH value of the buffer, monomers and crosslinkers are enriched on the surface of the protein by electrostatic force¹⁵³.

Proteins are vulnerable due to their complex structure and the presence of protease in blood circulation. The widely used approach to enhance stability is to modify the proteins with poly (ethylene glycol) (PEG). However, approximately 25% of patients have already developed anti-PEG antibodies before or after the first administration of PEG-modified proteins. Considering that zwitterionic polymers also can prevent quick clearance by macrophages, we designed nanocapsules with a layer of zwitterionic polymer, to resist non-specific protein absorption for long circulation time. 2-methacryloyloxyethyl phosphorylcholine (MPC) is selected as the monomer, which better shields the protein cores from serum protein adsorption under blood flow. Uricase was chosen as the model

enzyme. In mice injected with native uricase and uricase nanoparticles, uricase concentration in serum decreased dramatically after 8 h, while that with nanocapsules still remained the same. Thus, by coating proteins with a shell of zwitterionic polymer, a novel protein therapeutic protein delivery platform has been developed, with the ability to enhance protein stability, prolong half-life *in vivo* and reduce immunogenicity¹⁵⁴.

Central nervous system diseases are the leading cause of morbidity and mortality. The treatment, however, remains constrained by the blood brain barrier, which could block up ~98% of micro molecules and ~100% macromolecules. The BBB exhibits the receptor of choline and acetylcholine on the outside surface. Thus, a CNS delivery platform for protein delivery to the CNS was developed. The protein was encapsulated within nanocapsules, with monomer containing choline and acetylcholine analogues. BBB penetration of nanocapsules *in vivo* was evaluated in mice. Both dye-labelled n(BSA) and native BSA were injected in mice intravenously. Based on the one-compartment model, n(BSA) shows a half-life of 48.8 h, which is 6.3-fold of that of the native BSA (7.8 h). Fluorescent images further proved that a high accumulation of n(BSA) could be found in the brain area, which is 42-fold higher than that of the native BSA group¹⁵⁵.

3.1.4 Development of a novel LN-delivery nanocapsule targeting high endothelial venules (HEVs).

Herein, we develop a protein delivery nanocapsule with the targeting capacity of lymph node post intravenous administration based on the protein delivery platform. This nanocapsule takes usage of 2-Methacryloyloxyethyl phosphorylcholine (MPC) and N-(3-aminopropyl) methacrylamide (APM) as monomer. MPC is a hydrophilic neutral monomer, enabling increased stability and prolonged circulation time of the encapsulated protein,

while the amino group on APM provides the capability of surface modification. Together with the degradable crosslinker glyceryl dimethacrylate (GDMA), we grow a degradable shell of polymer network around the individual protein. With surface modification of MECA-79, nanocapsule enables specific accumulation in lymph nodes with a 19.3-fold higher than native protein *in vivo*. After systemically administered in engineered murine lymphoma model and human lymphoma model, the nanocapsules then slowly release the therapeutic monoclonal antibody rituximab (RTX), leading to a robust anti-lymphoma efficacy, and exhibit the potential for inhibiting metastasis by eliminating remnant cancer cells in the lymph node with a biosafety profile (**Fig. 3-1a**).

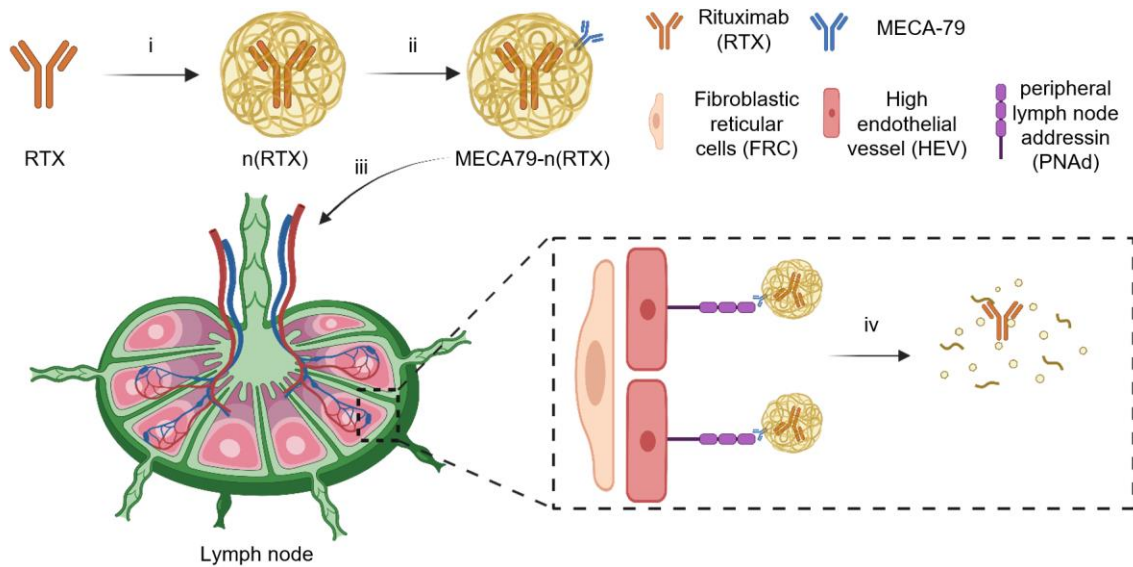


Fig. 3-1. A schematic illustration of the synthesis of the protein nanocapsule and its targeting efficacy to the lymph node. It mainly contained 4 steps: (i) 2-Methacryloyloxyethyl phosphorylcholine (MPC) monomer, N-(3-aminopropyl) methacrylamide (APM) and hydrolysable crosslinker glyceryl dimethacrylate (GDMA) gathered around RTX molecules and formed a thin shell of polymer. (ii) The MECA79 antibody was conjugated on n(RTX) via click chemistry reaction. (iii) After administrated

via intravenous injection, the protein nanocapsules which contained targeting ligands were combined on peripheral lymph node addressin (PNAd) on high endothelial vessels (HEVs) and enter lymph nodes. (iv) GDMA crosslinker cleaved and released RTX from the nanocapsule in the lymph nodes.

3.2 Materials and methods.

3.2.1 Materials.

All chemicals were purchased from Sigma-Aldrich (St. Louis, MO) unless otherwise noted and were used as received. Tetramethyl rhodamine (TAMRA) NHS ester was purchased from Lumiprobe (Hunt Valley, MD). Rituximab (RTX) was purchased from UCLA hospital pharmacy. Iscove's Modified Dulbecco's Medium (IMDM), RPMI 1640 medium and fetal bovine serum (FBS) were purchased from Corning (Corning, NY). Penicillin-streptomycin (PS) and zeocin were purchased from Thermo Fisher Scientific (West Hills, CA). Anti-human CD20 (2H7), anti-human CD107a (H4A3), MECA-79, anti-human IFN γ (MD-1), ELISA dilute buffer, TMB substrate set and HRP donkey anti-human IgG were purchased from Biolegend (San Diego, CA). Capture antibody for ELISA against rituximab (RTX) was purchased from Bio-Rad Laboratories (MCA2260, Hercules, CA). The ammonium-chloride-potassium (ACK) lysis buffer was purchased from quality biological (Gaithersburg, MD).

3.2.2 Instruments.

Images of cells and tissue sections were obtained with a Revolve R4 fluorescent microscope, Discover Echo Inc (San Diego, CA). Dynamic light scattering (DLS) studies of silicified cells were obtained by Zetasizer Nano instrument (Malvern Instruments Ltd.,

Kingdom). UV/vis absorbance was measured by NanoDrop One spectrophotometer (Thermo Fisher Scientific). The fluorescence intensity and absorbance were measured with an Infinite M200 Pro microplate reader (Tecan). Biomarkers on cell surface were measured by Attune flow cytometer (Thermo Fisher Scientific) and cell sorting was achieved by BD FACSAria III cell sorter (BD Biosciences). Cell numbers were acquired by manual counting with trypan blue dye exclusion under microscope. Optical and bioluminescent images were collected on IVIS Lumina II In vivo imaging system (PerkinElmer, Inc, Waltham, MA).

3.2.3 Synthesis of RTX nanocapsule.

RTX was first diluted in 1xPBS at a final concentration of 1 mg/ml. Diluted RTX was mixed with monomer MPC (20% m/v in PBS, MPC: RTX=16,000:1, n/n), monomer APM (10% m/v in PBS, APM: RTX=160:1, n/n) and degradable crosslinker GDMA (20% m/v in DMSO, GDMA: RTX=1600: 1, n/n) via vortex. The mixed solution was left at room temperature for 30 minutes and added APS (10% in m/v in PBS, APS: RTX=800: 1, n/n) and TEMED (20% in m/v in PBS, TEMED: APS=2: 1, w/w). The reaction mixture was mixed thoroughly and kept at 4°C for 2 hours and dialyzed in 1xPBS buffer to remove unreacted molecules. Nanocapsules were purified with hydrophobic interaction column (Phenyl-sepharose CL-4B) to remove unencapsulated RTX. CL-4B column was prepared in advance by adding 5 ml phenyl-sepharose CL-4B into column. The column was rinsed with 1x PBS three times and stored at 4°C. Before purification, the column needed to be rinsed with 10x PBS (20 ml). The unpurified nanocapsule was mixed with 20x PBS (1: 1, v/v), loaded in the rinsed column, and washed with 10x PBS 5 times. The purified

nanocapsules were dialyzed with 1x PBS buffer and concentrated with Amicon Centrifugal Filter Units (MWCO=30 kDa) for further use.

3.2.4 Determination of protein concentration.

The concentration of n(RTX) was determined by bicinchoninic acid (BCA) colorimetric protein assay. Briefly, native RTX was diluted to a series concentration of 500, 200, 100, 50, 20, 10, 5, 2, 1 $\mu\text{g/ml}$. BCA reagent mixture was made by mixing reagent A and B at the ratio of Reagent A: Reagent B= 50: 1. Then, each of the standards and samples were mixed with BCA mixture and incubated at room temperature for 30 minutes. The absorbance at 562 nm was determined with a UV/Vis spectrometer.

3.2.5 Synthesis of nanocapsules conjugated with MECA-79.

MECA-79 were conjugated on nanocapsules via copper-free click chemistry. Nanocapsules were diluted to 2 mg/ml, added into dibenzo-cyclooctyne-SS-N-hydroxysuccinimidyl ester (DBCO-SS-NHS) in DMSO (10 mg/ml, nanocapsule: DBCO-SS-NHS=1: 10, n/n) and incubated at 4°C for 4 hours. At the same time, MECA-79 antibody was added into NHS-PEG₄-azide (10 mg/ml, MECA-79: NHS-PEG₄-azide=1:10, n/n) and incubated at 4°C for 4 hours. Unreacted molecules were removed by dialysis with 1x PBS buffer overnight. The conjugation of DBCO modified nanocapsule and azide modified MECA-79 was then reacted at 4°C overnight at a molar ratio of 1: 1.

3.2.6 Determination of average number of conjugated ligands on nanocapsules.

Average number of conjugated ligands on nanocapsules was determined by measuring reacted DBCO. Briefly, the absorbance at 309 nm was measured in DBCO

modified nanocapsules and MECA-79 conjugated nanocapsules and number of reacted DBCO, or number of conjugated ligands was calculated based on the Beer-Lambert law as following formula:

$$\text{Number of DBCO per nanocapsule} = \frac{A_{309}}{\epsilon_{309} \times \text{conc of } n(\text{RTX})}$$

where A_{309} referred to absorbance of DBCO modified nanocapsules at 309 nm, and ϵ_{309} represents the extinction coefficient of DBCO at 309 nm, quantified as 12,000 $\text{M}^{-1}\text{cm}^{-1}$.

3.2.7 Zeta-potential and size measurement.

Zeta-potential and particle size were measured with Zetasizer Nano instrument. Purified nanocapsules were diluted in deionized water to a final concentration of 0.5 mg/ml and measured three times for each group.

3.2.8 Cell culture.

2F7-BR44 cell line was obtained from lab stock as previously described⁷⁶. Briefly, 2F7 cells were transduced with lentiviral vectors encoding mCherry and luciferase under ubiquitin C promoter. Transduced 2F7 cells were sorted, sub-cloned to obtain single cell clones and finally selected 2F7-BR44 single clone after in vivo selection for brain metastasis lymphoma. 2F7-BR44 cells were cultured in IMDM with 15% FBS, 1% glutamine, 1% penicillin-streptomycin and 100 mg/ml zeocin at 37°C.

A20-hCD20 and A20 cells were cultured in RPMI 1640 supplemented with 10% FBS, 1% glutamine and 1% penicillin-streptomycin at 37°C.

3.2.9 Lymphoma model setup and progression monitoring in vivo.

Animal research described in the study was approved by the University of California, Los Angeles' Chancellor's Animal Research Committee (Institutional Animal Care and Use Committee) and was conducted in accordance with guidelines for the housing and care of laboratory animals of the National Institutes of Health and Association for Assessment and Accreditation of Laboratory Animal Care International. For A20-hCD20 murine lymphoma model, 0.5 million A20-hCD20 cells were injected into BALB/cJ mice via the lateral tail vein. Mice were euthanized in week four. For the 2F7-BR44 human lymphoma model, one million 2F7-BR44 cells were injected into nude mice intravenously via tail vein. Lymphoma formation and progression was monitored every week by IVIS Lumina II In Vivo Imaging System. Mice were anesthetized with isoflurane, and intraperitoneally injected with 3 mg luciferin (Pierce). Bioluminescent signals were obtained 5 minutes later. Tumor burden was quantified as the total photon flux per second within the region of interest (ROI).

3.2.10 Biodistribution studies.

The biodistribution of nanocapsules was analyzed by IVIS Lumina II In Vivo Imaging System. BALB/cJ mice were first inoculated with A20-hCD20 cells and randomly separated into four groups. Native RTX was first labeled with TAMRA fluorescent dye and RTX nanocapsules were synthesized and purified as described above and administered to mice (10 mg/kg). Mice were euthanized and perfused with pre-chilled 1x PBS buffer. Fluorescent signals from ex-vivo organs were obtained via IVIS Lumina II. Tissues were then homogenized with closed system micro tissue homogenizer (DWK) and supernatant was collected after centrifuge. Labeled native RTX was diluted to a series concentration of

500, 200, 100, 50, 20, 10, 5, 2, 1, 0.5, 0.2 µg/ml and measured with microplate reader to set up the standard curve.

3.2.11 Pharmacokinetics studies.

The pharmacokinetics of RTX nanocapsules was investigated in A20-hCD20 tumor-bearing BALB/cJ mice. Inoculated mice were randomly separated into three groups and intravenously injected with TAMRA labeled native RTX, n(RTX) or MECA79-n(RTX) with the RTX dosage of 10 mg/kg. The blood samples were collected and centrifuged at 1,500 rpm for 5 min. Supernatant plasma was collected and fluorescence signals at different time points were determined with microplate reader.

3.2.12 Monoclonal antibody detection by ELISA.

ELISA plates were first incubated with 1 mg/ml of anti-RTX antibody at 4 °C overnight. Plates were rinsed with PBST three times to remove coating solution, added 200uL 3% BSA in PBS buffer and incubated for 2 hours at room temperature. Animal body fluids and tissue homogenates containing encapsulated RTX in non-degradable nanocapsules were treated with 100 mM sodium acetate buffer (pH 5.4) at 4 °C overnight, then used for ELISA measurement. Diluted samples and standards (1-500 ng/ml) were added in washed wells and incubated at 4 °C overnight. Triplicates were performed for each sample. Plates were washed with PBST three times to remove unbound samples. HRP-conjugated anti-human Fc antibody was added and incubated for 1 hour at room temperature. The substrate working solution was prepared by mixed TMB substrate A with TMB substrate B as instructed by the guideline. After washing three times with PBST, a prepared substrate working buffer was added into each well and incubated for 15 minutes.

The reaction was stopped and the absorbance at 450 nm was measured with a microplate reader.

3.2.13 Cytotoxicity assay.

Cytotoxicity profiles of materials, native RTX or RTX nanocapsules were assessed by counting cell number with Attune flow cytometer. For material cytotoxicity test, 2F7-BR44 cells were spun down, re-suspended with BSA nanocapsule solutions at different concentrations and seeded in 24-well plates (5×10^5 cells per well). After incubation for 24 hours, 200 μ l medium was taken from each well and cell number was counted. For complement-dependent cytotoxicity (CDC) test, 2F7-BR44 cells were cultured for 24 hours with native RTX or RTX nanocapsules at a RTX dosage of 20 μ g/ml, together with 20% human serum with no heat inactivation. For antibody-dependent cellular cytotoxicity (ADCC) test, 2F7-BR44 cells were cultured native RTX or RTX nanocapsules at a RTX dosage of 20 μ g/ml, together with PBMC at a ratio of 2F7-BR44: PBMC= 1:5. The mCherry positive live cells were denoted as live 2F7-BR44 cell and cell viability was calculated as following formula:

$$\text{Cell viability (\%)} = \frac{\text{Live cell number after treatment}}{\text{Live cell number without treatment}} \times 100\%$$

3.2.14 Anti-tumor efficacy of RTX in murine lymphoma model.

A20-hCD20 cells (5×10^5 cells per mouse) were injected intravenously via the lateral tail vein into BALB/cJ mice. Seven days after inoculation, mice were treated with five continuous doses of native RTX, n(RTX) or MECA79-n(RTX) with the RTX dosage of 5 mg/kg on Day 7, 8, 9, 10 and 11, as indicated group and schedule. Mice were sacrificed when in a critical condition due to the lymphoma burden or at the end of timepoint

predetermined in experimental design. Mice were perfused with pre-chilled PBS and euthanized. Organs were then harvested and grounded into single-cell suspension. Isolated single cells from tissues were used to measure tumor burden, by staining with anti-human CD20 and testing with flow cytometry.

3.2.15 Metabolic pathway analysis.

A respirometry assay was performed on a Seahorse XFe24 Extracellular Flux Analyzer (Agilent Technologies) at the Mitochondria and Metabolism Core in UCLA. Single cell suspension from ex-vivo organs was stained with APC-Cy7 anti-human CD20 and sorted in the UCLA Flow Cytometry Core Facility with FACS Aria II (BD Biosciences). Briefly, on the day prior to assay, sorted cells were seeded in coated Seahorse XF24 microplate (1.5×10^5 cells per well). The assay medium was prepared by adding 2 mM pyruvate, 2 mM glutamine and 8 mM glucose in DMEM medium. On the day of assay, cells were centrifuged down to the bottom of the plate, rinsed twice and incubated with 500 μ l assay buffer for 30 minutes in a non-CO₂ incubator together with 3 μ M etomoxir, 5 μ M BPTES and 5 μ M UK5099. During the assay, oligomycin (2 μ M), FCCP (0.9 μ M), antimycin (2 μ M) and rotenone (2 μ M) were added as instructed by the guideline. Basal OCR was calculated as the average of the two measurements before injection of oligomycin.

3.2.16 Anti-tumor efficacy of RTX in human lymphoma model in mice.

2F7-BR44 cells (1×10^6 cells per mouse) were injected intravenously via the lateral tail vein into nude mice. Seven days after inoculation, mice were treated with five continuous doses of native RTX, n(RTX) or MECA79-n(RTX) with the RTX dosage of 5 mg/kg on Day 7, 8, 9, 10 and 11, as indicated group and schedule. Mice were sacrificed

when in a critical condition due to the lymphoma burden or at the end of timepoint predetermined in experimental design. Mice were perfused with pre-chilled PBS and euthanized. Organs were then harvested and grounded into single-cell suspension. Isolated single cells from tissues were used to measure tumor burden, by measuring mCherry expression on 2F7-BR44 cells by flow cytometry.

3.2.17 Systemic toxicity.

The major organs, including heart, liver, spleen, kidney, and lung were collected at endpoint and fixed in 4% paraformaldehyde for H&E histological analysis by UCLA Translational Pathology Core Laboratory.

3.2.18 Statistics.

Data are presented as means \pm S.D. unless otherwise indicated. Statistical significance was calculated using GraphPad Prism. The significance of survival curve data was compared by a two-way ANOVA test. All the other comparisons of significance between groups were calculated by two-tailed unpaired t-test. The P values of 0.05 or less are considered significant.

3.3 Results.

3.3.1 MECA-79 modified nanocapsule induces specific accumulation in Lymph nodes.

We previously developed a protein delivery platform where the individual protein is encapsulated within a thin polymer shell via in situ polymerization of monomers with together with stimuli-responsive crosslinkers⁷⁶. To encapsulate RTX, 2-methacryloyloxyethyl phosphorylcholine (MPC, serving as monomer) and glyceryl dimethacrylate (GDMA, serving as a degradable crosslinker) aggregated around RTX

molecules. 1% N-(3-aminopropyl) methacrylamide (APM) is also involved as a source of amino group for subsequent surface modification. This aggregation is driven by non-covalent interactions, forming a thin polymer shell initiated by ammonium persulfate (APS) and N, N, N', N'-Tetramethyl ethylenediamine (TEMED). The encapsulation process results in the formation of RTX nanocapsules, denoted as n(RTX). n(RTX) and MECA-79 antibodies were then conjugated via click chemistry and modified nanocapsules were denoted as MECA79-n(RTX). The modified nanocapsules exhibited a uniform size of around 30 nm (**Fig. 3-2 a**). While the native RTX averaged 9.4 nm in size, the n(RTX) and MECA79-n(RTX) exhibited an average size of 28.9 nm and 35.5 nm, respectively (**Fig. 3-2 b**). Also, the shift in surface charge from a positive value (native RTX, +7.649 mV) to neutral values (n(RTX) at +0.39 mV and MECA79-n(RTX) at +0.25 mV) suggested a successful encapsulation (**Fig. 3-2 c**). Furthermore, we measured the encapsulation with protein gel electrophoresis, where n(RTX) and MECA79-n(RTX) remained in stacking gel due to their large molecular weight, while native RTX was in separating gel (**Fig. 3-2 d**).

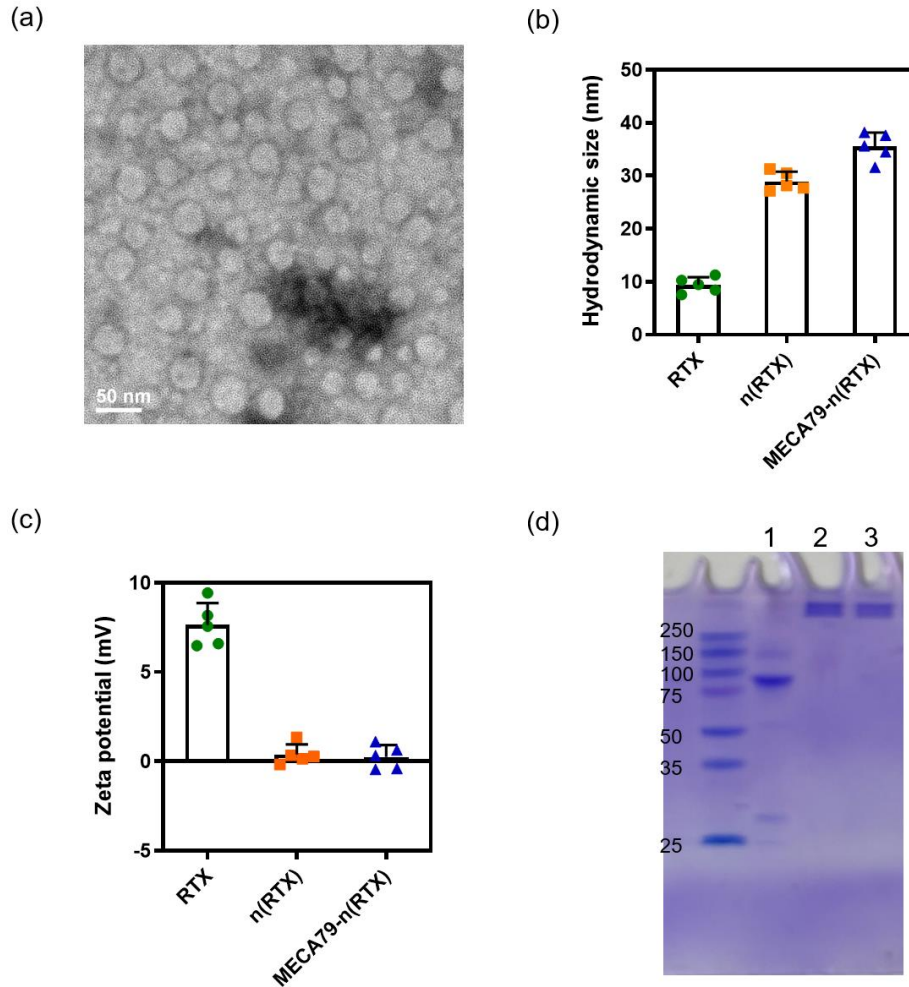


Fig. 3-2. Characterization of MECA79 modified nanocapsules. **a**, TEM image of MECA79-n(RTX). Scale bar = 50 nm. **b-c**, Hydrodynamic size (**b**) and zeta potential (**c**) of native RTX, n(RTX) and MECA79-n(RTX) (n=5). **d**, Sodium dodecyl sulfate-polyacrylamide gel electrophoresis (SDS-PAGE) patterns of protein and nanocapsules. Data are presented as means \pm S.D.

Then, we examined the lymph-node (LN) targeting efficacy in lymphoma bearing BALB/cJ mice with model protein BSA, labeled with the fluorescent dye TMR. Mice were first inoculated with the A20-CD20 cell, which was a murine lymphoma cell line with human CD20 expression on the surface. Then, mice were randomly separated into four

groups and injected intravenously with a single dose of native BSA, n(BSA), IgM-n(BSA) or MECA79-n(BSA) via lateral tail vein. After 24 hours, the main organs were collected after perfusion and imaged with IVIS Lumina II. As shown in **Fig. 3-3 a**, all nanocapsules improved the half-life of encapsulated BSA, resulting in an increase in total fluorescent intensity compared to native BSA. Among all treatments, only MECA79-n(BSA) exhibited strong accumulation in lymph nodes of mice. The significant improvement in targeting LNs with MECA79 modification was quantitatively compared to targeting with no conjugation or with no conjugation or isotype IgM conjugation (**Fig. 3-3 b**). In contrast, similar levels of accumulation were observed among the four samples in non-targeted organs, including the liver and kidneys (**Fig. 3-3 c**). In our previous study¹⁵⁵, we observed that nanocapsules synthesized with MPC enabled the delivery of proteins into the central nervous system (CNS). With the modification of MECA-79 antibodies, MECA79-n(BSA) exhibited decreased accumulation in the brain due to the increased particle size and improved LN targeting (**Fig. 3-3 d**). For a quantitative comparison among all samples for LN targeting accumulation, we calculated the ratio of fluorescent intensities between the LNs and the liver to assess their preferential localization. As the data showed in **Fig. 3-3e**, LNs/Liver ratios in MECA79-n(BSA) group were 2.30-fold, 2.08-fold, and 2.80-fold compared to those in the native BSA group, n(BSA) group and IgM-n(BSA) group, respectively. Additionally, we determined the overall accumulation in the lymph node by constructing a standard curve based on fluorescence measurements. Overall accumulation in lymph nodes in the MECA79-n(BSA) group was 19.3-fold, 16.2-fold, and 18.2-fold higher than that in the native BSA group, n(BSA) group and IgM-n(BSA) group, respectively (**Fig. 3-3 f**).

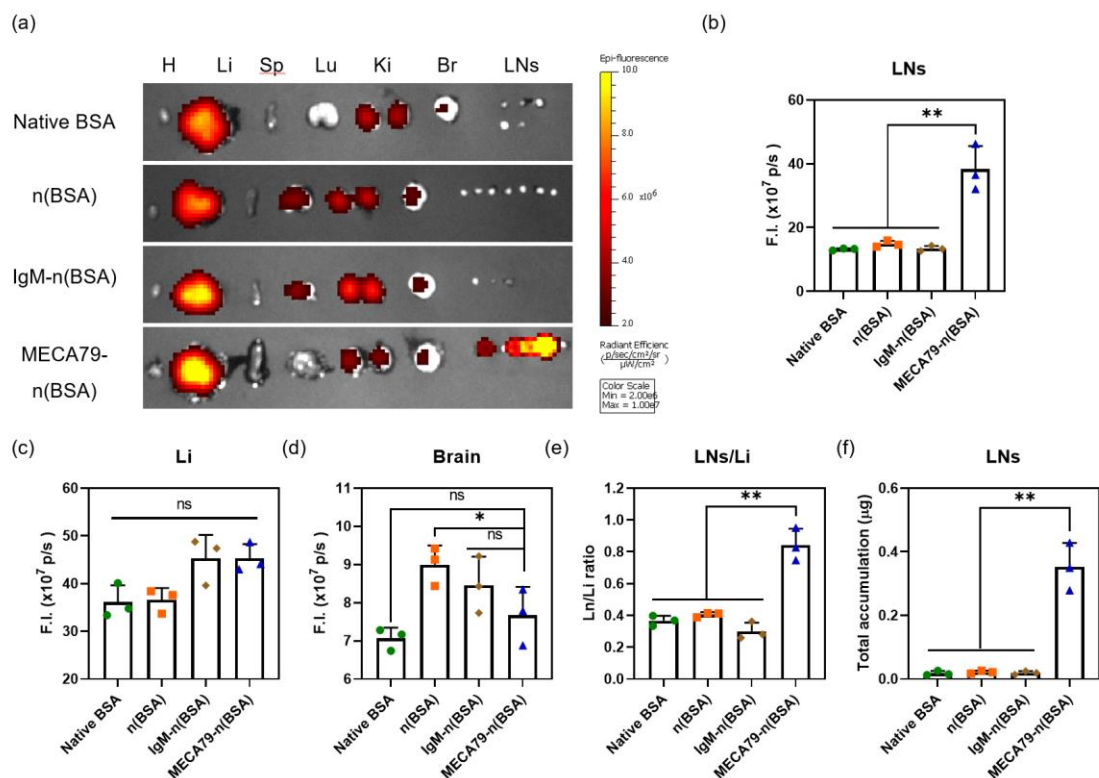


Fig. 3-3. MECA-79 modification on nanocapsule induced specific accumulation in lymph nodes. **a**, Lymphoma-bearing mice (n=3) were administered 10 mg/kg TAMRA labeled native BSA, n(BSA), IgM-n(BSA) and MECA79-n(BSA) via the tail vein. Mice were sacrificed and perfused ex vivo images were collected by IVIS 24 h post administration. **b-d**, Fluorescence intensity of TMR-labeled BSA in lymph node (b), liver (c) and brain (d). **e**, Fluorescence intensity ratio of lymph node versus the liver. **f**, Protein concentration in lymph nodes in different groups. Data are presented as means \pm S.D. H, heart. Li, liver. Sp, spleen. Lu, lung. Ki, kidney. Br, brain. LNs, lymph nodes.

3.3.2 Encapsulation and surface modification retains the anti-tumor efficacy of monoclonal antibody.

The in vitro cytotoxicity of nanocapsules was then evaluated with 2F7-BR44 cells by counting live cell numbers. The 2F7-BR44 cell line is a single clone derived from the

parental DLBCL line, isolated from brain tissue of the xenografted immunodeficient mice. We further genetically modified the 2F7-BR44 cells with lentiviral vectors to express an mCherry-luciferase fusion protein, serving as a live cell marker to monitor cell viability. The cells were first treated with a series of concentrations of MECA79-n(BSA) for 24 hours. As the data showed in **Fig. 3-4 a**, no obvious cytotoxicity was detected in any concentration, suggesting that both encapsulation and surface modification had no effect on cell viability. The cytotoxicity of rituximab to DLBCL cells was exerted through several mechanisms, including direct apoptosis, complement-dependent cytotoxicity (CDC), and antibody-dependent cellular cytotoxicity (ADCC)¹⁵⁶. When 2F7-BR44 cells were individually incubated with different samples as designed, cytotoxic effects were found in both n(RTX) and MECA79-n(RTX) groups, with the lower cytotoxicity compared to the native RTX group being attributed to the necessary time to release (**Fig. 3-4 b**). 2F7-BR44 cells were incubated with samples together with human serum without heat activation. In all groups with serum added, cell viability was 48.2% in n(RTX) group and 48.3% in MECA79-n(RTX) group, compared to 99.98% in PBS group (**Fig. 3-4 b**). To measure the capability to induce ADCC of RTX nanocapsules, 2F7-BR44 cells were incubated with nanocapsules together with human PBMCs. In the PBS group, 2F7-BR44 cells exhibited a cell viability of 79.9% in the presence of PBMCs, indicating the PBMCs themselves induced cell death. As compared to PBS group, a significantly enhanced cell killing efficacy was found in native RTX, n(RTX) and MECA79-n(RTX) group, with a cell viability percentage of 13.9%, 7.82% and 8.21%, respectively (**Fig. 3-4 c**). We further evaluated the expression of ADCC-related cytokine and surface marker on 2F7-BR44 cells. Compared to the PBS group, IFN γ expression increased from 1.77% to 2.68% and CD107a

expression increased from 4.67% to 8.25% in the MECA79-n(RTX) group (Fig. 3-4 d, Fig. 3-4 e). These results demonstrated that encapsulation and surface modification exhibited no obvious material cytotoxicity and retained the anti-lymphoma efficacy of therapeutic antibody RTX.

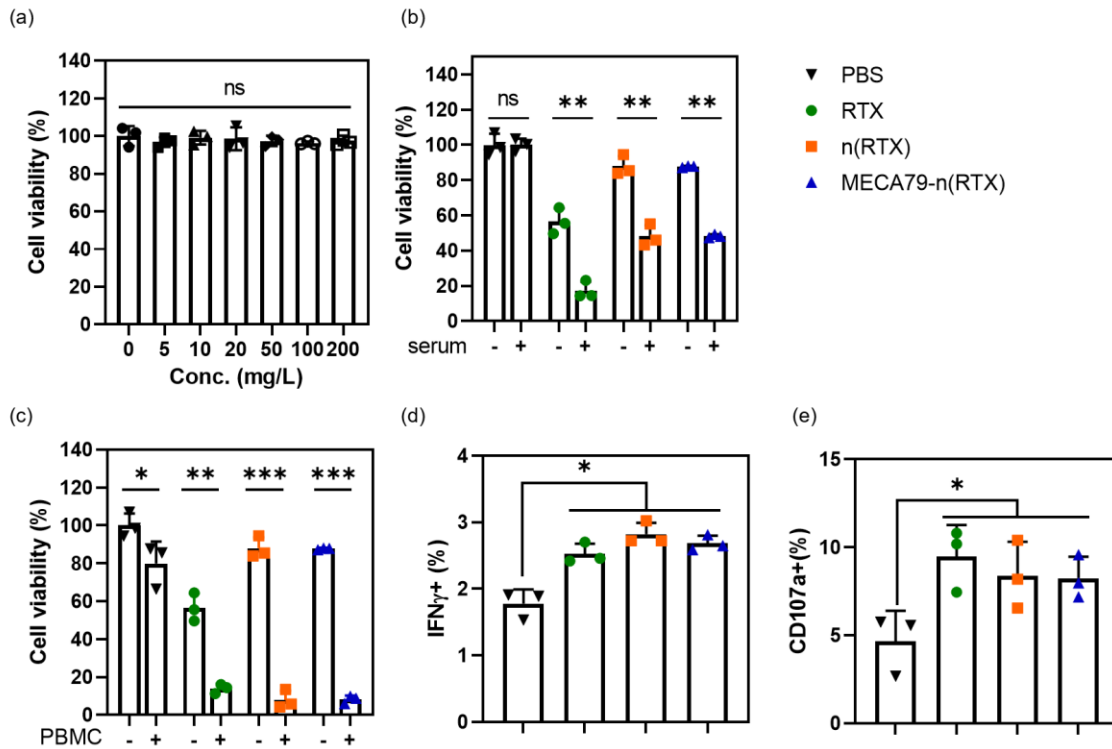


Fig. 3-4. Encapsulation and surface modification retained the anti-tumor efficacy of the monoclonal antibody. **a**, In vitro cytotoxicity of n(BSA) at different concentrations. **b**, Cell viability of different groups in the presence or absence of serum. **c**, Cell viability of different groups in the presence or absence of PBMC. **d-e**, IFN γ (d) and CD107a (e) expression level on tumor cells after incubation with different groups. Data are presented as means \pm S.D (n=3). Statistical significance was determined by a two-tailed t-test. *P<0.05, **P<0.01, ***P<0.001

3.3.3 MECA-79 modified nanocapsules suppress tumor progression and obstruct lymph-node mediated metastasis.

To evaluate the anti-tumor efficacy, BALB/cJ mice were engrafted with A20-hCD20 cells, a murine lymphoma cell line with human CD20 expressed on the surface, enabling treatment with the clinically used therapeutic monoclonal antibody RTX. For in vivo therapy, mice bearing A20-hCD20 tumors were randomly divided into four groups, which are PBS group, native RTX group, n(RTX) group and MECA79-n(RTX) group. Except for the PBS group, mice in the other three groups were intravenously administered at a RTX dosage of 5 mg/kg from Day 7 to Day 11. Mice were sacrificed when they lost 20% of their body weight or on day 28 (**Fig. 3-5 a**). We evaluated the survival rates using Kaplan-Meier in all four groups. As shown in **Fig. 3-5 b**, compared to PBS group, native RTX and n(RTX) increased median survival time from 10 days to 15 days, with all mice dead from tumor progression by Day 18. In contrast, by the end of day 28, four out of six mice in the MECA79-n(RTX) group survived, indicating that MECA-79 modified nanocapsules significantly improved mouse life span.

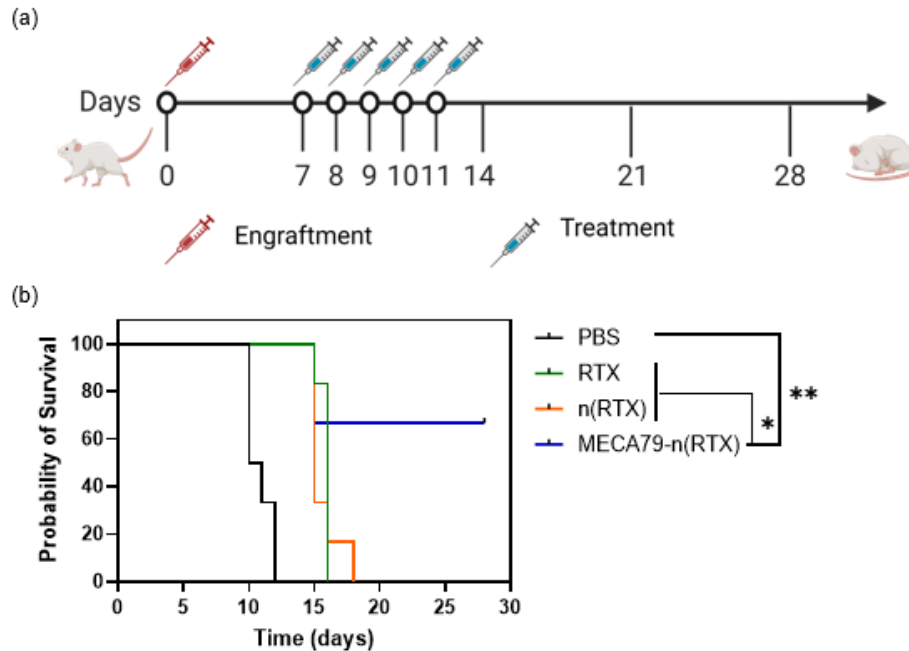


Fig. 3-5. MECA79-n(RTX) suppressed lymphoma progression in murine lymphoma model. **a**, Schematic of in vivo study design of modified nanocapsule in murine lymphoma model. **b**, BALB/cJ mice (n=6) intravenously inoculated with 5×10^5 A20-hCD20 lymphoma cells were treated with RTX encapsulated nanocapsules (1 mg/kg per dose) on Day 7, 8, 9, 10 and 11. Kaplan-Meier survival curve was shown. Statistical significance was determined by a two-way ANOVA test.

To evaluate the obstruction of lymph-node mediated metastasis, A20-hCD20 lymphoma bearing mice were randomly separated into four groups, which are week 1, week 2, week 3 and week 4, and mice were sacrificed at the designated time. As shown in Fig. 3-6, from week 1 to week 4, the percentage of lymphoma cells decreased from 12.1% to 6.03% in lymph nodes, while increasing from 2.89% to 17.9% in the liver, from 5.97% to 22.7% in the spleen, respectively, providing evidence that lymphoma was first located

in the lymph nodes and then subsequently metastasized to distant organs (liver and spleen) in this lymphoma mouse model.

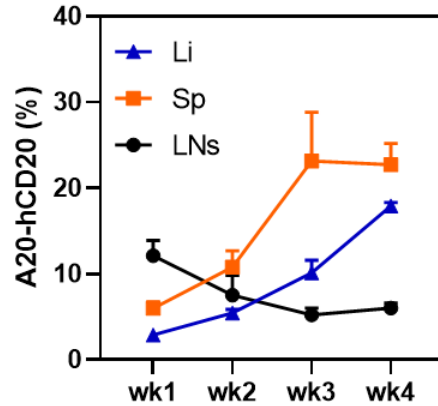


Fig. 3-6. A20-hCD20 ratio in organs (lymph nodes, liver, spleen) at different time points.

Given that A20-hCD20 lymphoma model exhibited a metastasis pattern, we further measured lymphoma burden in different organs. Compared to the other treatment groups, mice treated with MECA79-n(RTX) exhibited lower tumor burden in both the primary site (LNs, **Fig. 3-7 a**), metastatic pathway (**lymph, Fig. 3-7 b**) and metastatic sites (bone marrow and liver and spleen, **Fig. 3-7 f-h**). Therefore, MECA-79 modified nanocapsules inhibited tumor progression and reduced lymph-node mediated metastasis by removing remnant tumor cells in lymph nodes.

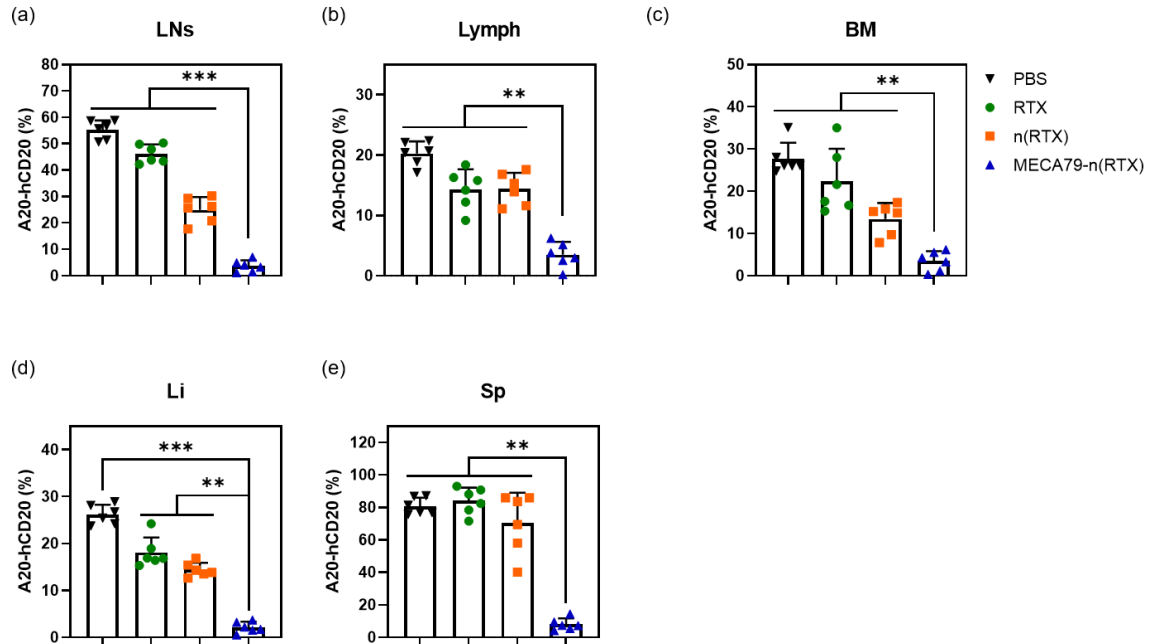


Fig. 3-7. MECA79-n(RTX) reduced tumor burden in both primary sites and metastasis sites. a-b, Tumor burden in primary site (lymph node, a) and metastatic pathway (lymph, b). **c-e,** Tumor burden in distant organs, including bone marrow (c), liver (d) and spleen (e). Data are presented as means \pm S.D. Statistical significance was determined by a two-tailed t-test. * $P<0.05$, ** $P<0.01$, *** $P<0.001$. LNs, lymph nodes. Sp, spleen. BM, bone marrow. Li, liver.

To further validate that MECA79-n(RTX) possessed the potential to reduce lymph-node mediated metastasis, we measured the metabolomics preference of tumor cells. The lymph-node metastatic tumors showed higher accumulation of fatty acid than the primary tumors, forcing the adapted cells to have a metabolic preference for fatty acid, rather than glutamine or glucose¹⁵⁷. Etomoxir is an inhibitor of carnitine palmitoyltransferase-1 (CPT-1), which is an essential enzyme in the fatty acid oxidation process. Thus, etomoxir is the model compound to block fatty acid oxidation by inhibiting CPT-1. The lower oxygen consumption rate (OCR) after adding etomoxir indicated a higher dependency on fatty acid

oxidation. After mice were sacrificed, the spleen was collected after perfusion and A20-hCD20 lymphoma cells were sorted for further metabolomic analysis with Seahorse XFe24 Extracellular Flux Analyzer. As the data showed in **Fig. 3-8**, basal OCR in parental A20-hCD20 cells was 130.08 pmol/min, while the OCR in native RTX and n(RTX) treated cells were 100.79 pmol/min and 85.29 pmol/min, respectively, indicating cells in spleen came from lymph-node associated metastasis pathway, and encapsulation itself exhibited limited efficacy to obstruct metastasis. Whereas, basal OCR in MECA79-n(RTX) was 126.08 pmol/min, significantly increased compared to the OCR in the native RTX group and n(RTX) group, illustrating that MECA79-n(RTX) had the potential to reduce lymph-node mediated metastasis.

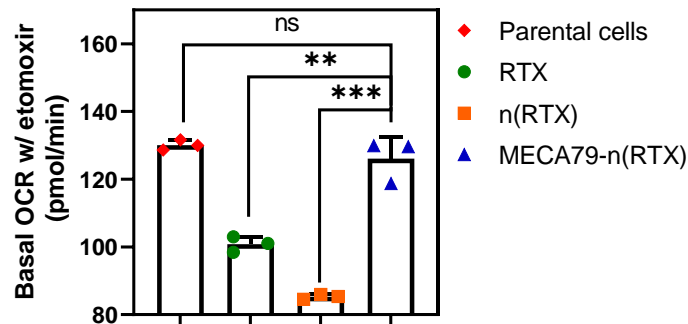


Fig. 3-8. Metabolic dependency of fatty acid involved pathway in different groups (n=3). Data are presented as means \pm S.D. Statistical significance was determined by a two-tailed t-test. ns, no significance, *P<0.05, **P<0.01, ***P<0.001.

3.3.4 MECA-79 modified nanocapsules inhibit human non-Hodgkin lymphoma progression.

Next, we compared the anti-tumor efficacy of MECA79-n(RTX) in a human NHL model. For the *in vivo* therapy, nude mice were intravenously injected with 2F7-BR44 cells with expression of mCherry-luciferase fusion protein for further tumor progression monitoring. Mice were then randomly divided into five groups, including PBS group, native RTX group, IgM-n(RTX) group, MECA79-n(BSA) group and MECA79-n(RTX) group. Seven days post engraftment, mice were injected with PBS buffer or various samples at a protein dosage of 5 mg/kg from Day 7 to Day 11 (Fig. 3-9 a). Tumor progression was monitored by IVIS every week and mice were sacrificed when bioluminescence intensity from the whole body reached 1×10^9 p/sec/cm²/sr (Fig. 3-9 b).

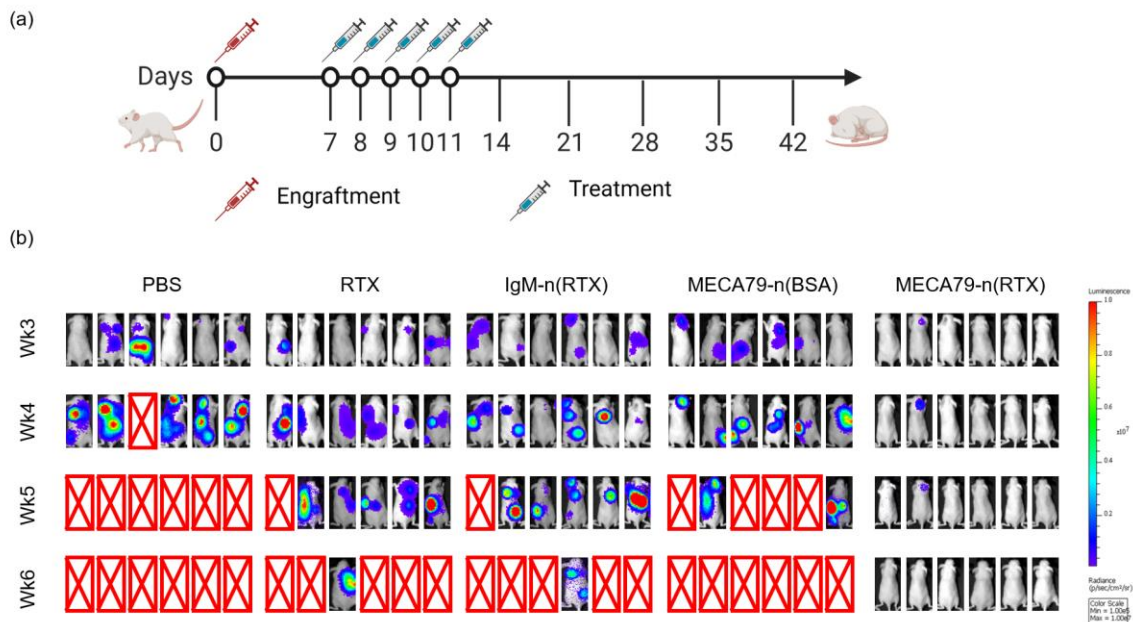


Fig. 3-9. Modified nanocapsule inhibited human non-Hodgkin lymphoma progression.

a, Schematic of *in vivo* study design of the modified nanocapsule in the human non-Hodgkin lymphoma model. **b**, Nude mice inoculated with 1×10^6 2F7-BR44 lymphoma

cells were treated with RTX encapsulated nanocapsules (1 mg/kg per dose) on Day 7, 8, 9, 10 and 11. Tumor progression was monitored with IVIS weekly. Tumor growth was shown.

Animal survival was also evaluated in all five groups. MECA79-n(RTX) showed a significant inhibition of tumor progression, with no mouse mortality by the end. Compared to the PBS group, MECA79-n(BSA) failed to prolong the lifespan, indicating that encapsulation and surface modification didn't have the capability to inhibit cancer. Both RTX group and IgM-n(RTX) group exhibited a moderate anti-lymphoma efficacy with no difference between these two groups, resulting from surface modification with the isotype control protein lacking the ability to direct nanocapsules to lymph nodes (**Fig. 3-10 a**). Quantitative bioluminescent signals further provided evidence proving that MECA79-n(RTX) offered the most efficient anti-tumor efficacy (**Fig. 3-10 b**).

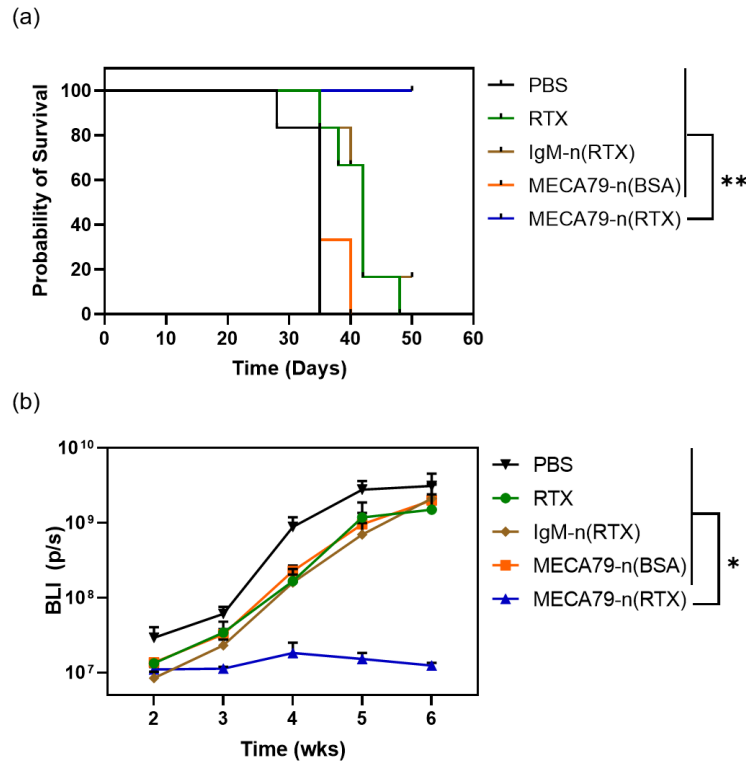


Fig. 3-10. Modified nanocapsule inhibited human NHL lymphoma progression and prolonged lifespan. a, Nude mice inoculated with 1×10^6 2F7-BR44 lymphoma cells were treated with RTX encapsulated nanocapsules (1 mg/kg per dose) on Day 7, 8, 9, 10 and 11. Kaplan-Meier survival curve of mice was shown. Statistical significance was determined by a two-way ANOVA test. **b,** Bioluminescence values in vivo in different groups. *P<0.05, **P<0.01.

In addition, body weights in all five groups showed no obvious changes, indicating a good biocompatibility and low toxicity of MECA79-n(RTX) (**Fig. 3-11**).

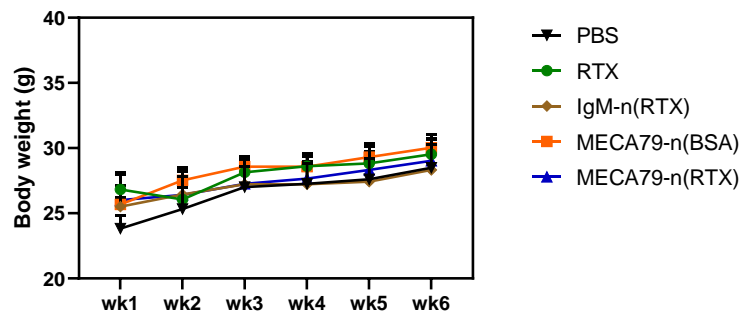


Fig. 3-11. Body weight of treated 2F7-BR44 bearing nude mice (n=6). Data are presented as means \pm S.D.

By the end of the study, metastasis sites (brain and bone marrow) were collected post perfusion. Consistent with the tumor progression profile, MECA79-n(RTX) exhibited a lower mCherry expression from 2F7-BR44 cells in comparison to the other four groups (Fig. 3-12 a-b).

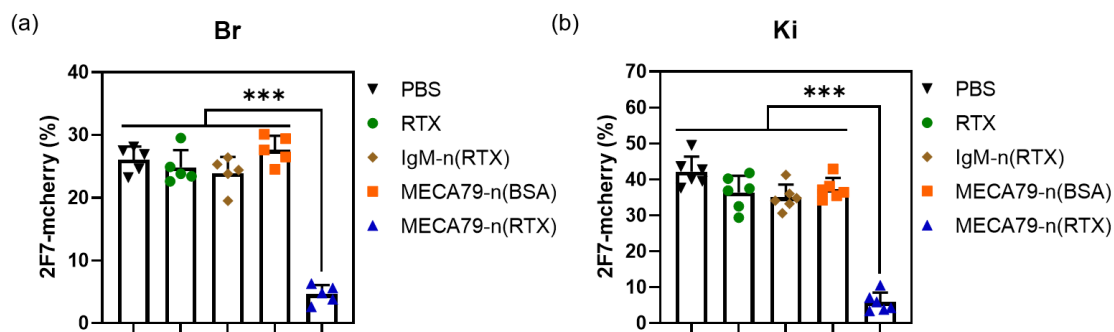


Fig. 3-12. MECA79-n(RTX) reduced tumor burden in distant organs. Tumor load in brain (a) and kidney (b) at the endpoint. Data are presented as means \pm S.D. Statistical significance was determined by a two-tailed t-test. * $P < 0.05$, ** $P < 0.01$, *** $P < 0.001$

3.3.5 Modified nanocapsules exhibit a biosafety profile.

The systemic toxicity was then investigated. The hematoxylin and eosin (H&E) staining for the major organs was performed. No significant pathophysiological changes were found in MECA79-n(RTX) group, demonstrating a biosafety profile *in vivo*. As shown in the H&E staining result of the kidney, obvious tumor nests were found in the PBS group and RTX group, however, no obvious tumor was exhibited in the MECA79-n(RTX) group, further proving the efficient inhibition of tumor progression (**Fig. 3-13 a**). Subsequently, we assessed the liver and renal function in treated groups by measuring the levels of aspartate transaminase (AST), alanine transaminase (ALT), blood urea nitrogen (BUN) and uric acid in blood stream. MECA79-n(RTX) showed no significant systemic toxicity (**Fig. 3-13 b-c**). Therefore, MECA79-n(RTX) exhibited good biocompatibility and a biosafety profile *in vivo*.

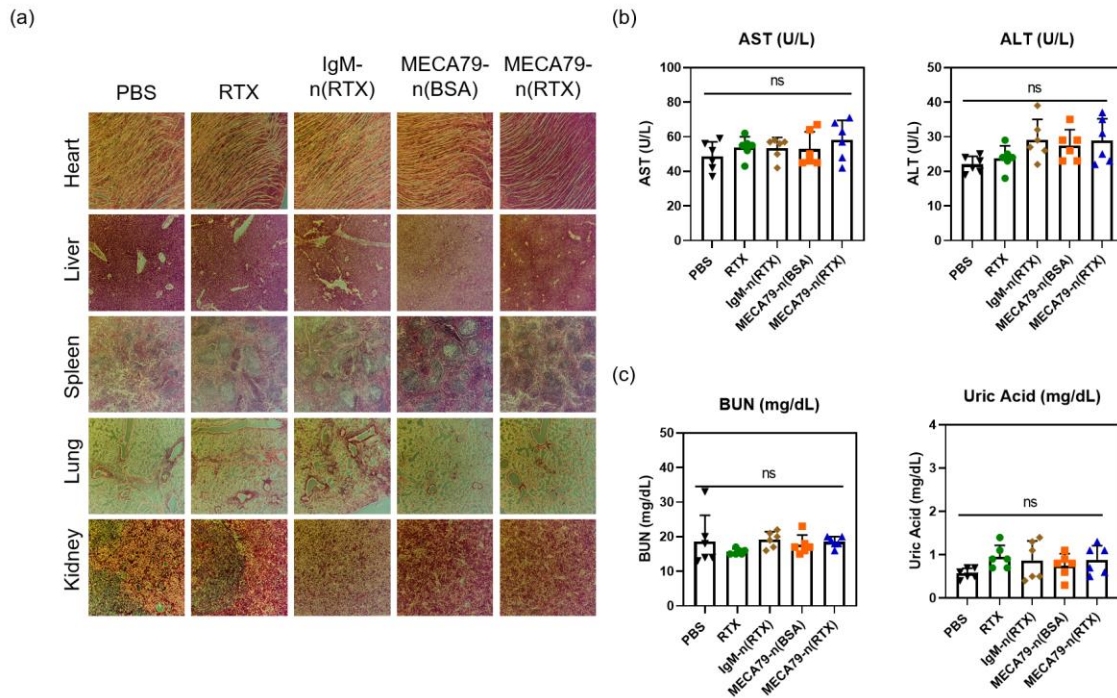


Fig. 3-13. Evaluation of systemic toxicity. **a**, Pathology analyses of major organ sections from mice by H&E staining. **b-c**, Hepatic (b) and renal (c) function assessment of nude mice. Data are presented as means \pm S.D. Statistical significance was calculated by t-test. ns, no significance. AST, Aspartate transaminase. ALT, Alanine transaminase. BUN, blood urea nitrogen.

3.4 Conclusion and discussion.

We developed an MPC-based degradable RTX nanocapsule, enabling prolonged systemic circulation, stable polymer shell while releasing through gradual hydrolysis. Modification with MECA-79 antibody results in a 19.3-fold higher specific accumulation of n(RTX) in lymph node in comparison to native RTX. Encapsulation and surface modification retained anti-tumor efficacy of therapeutic antibody RTX. Consistent with the enhanced RTX concentration in lymph nodes, MECA79-n(RTX) significantly reduced lymphoma burden in the lymph nodes. The lower percentage of tumor cells in metastasis

sites and lymph fluid provides the potential to obstruct metastasis pathway. Notably, the encapsulated protein was substitutable, which provides a feasible method to satisfy diverse medical needs.

Rituximab is a first-line treatment for non-Hodgkin lymphoma; however, it is insufficient to eliminate tumor cells hiding in lymph nodes, which may induce the potential risk of tumor relapse. Given that the lymph node is essential in tumor metastasis and the initiation and regulation of adaptive immune responses, it's of great importance to deliver treatments into lymph nodes to enhance therapeutic outcomes or immune responses. However, current lymph-node targeting strategies still face critical obstacles: (1) Opposite characterization requirements of nanocarriers for interstitium transfer and lymph node retention; (2) Uneven distribution of treatments with generally used peripheral administration; (3) Current lymph-node targeting strategies carry small molecules. Thus, we propose an MPC-based degradable RTX nanocapsule, enabling prolonged systemic circulation, stable polymer shell while releasing through gradual hydrolysis (**Fig. 3-2**). Modification with MECA-79 antibody results in a 19.3-fold higher specific accumulation of n(RTX) in lymph node in comparison to native RTX (**Fig. 3-3**). Encapsulation and modification retain the main action mechanisms of RTX, including apoptosis, antibody-dependent cell-mediated cytotoxicity (ADCC), and complement dependent cytotoxicity (CDC) (**Fig. 3-4**).

To mimic lymphoma progression in clinical patients, we first utilize A20-hCD20 murine lymphoma mouse model. A20 cells are transduced with lentiviral vectors to express human CD20 on the surface, enabling treatment with the FDA-proved monoclonal antibody rituximab. Also, the A20-hCD20 mouse model exhibits a metastasis trend from

primary site (lymph node) to distant organ (liver and spleen), which mimics the common metastasis sites in the clinic (**Fig. 3-6**). Within the murine lymphoma model in BALB/cJ mice, MECA79 modified nanocapsules sufficiently inhibit both primary and metastatic sites (**Fig. 3-5, 3-7**). Pharmacodynamics in the human lymphoma mice model also provides evidence that MECA79 modified nanocapsules eliminate tumor progression with a biosafety profile (**Fig. 3-9 to 3-13**).

Chapter 4: Summarization and perspective.

The global burden of lymphoma varies significantly across regions, influenced by demographic and geographic factors. Non-Hodgkin lymphoma (NHL) is the seventh most common cancer in the United States and ranks sixth in cancer mortality. Its high prevalence and mortality rates underscore the need for effective treatment strategies and a deeper understanding of its epidemiology. The prognosis for NHL patients is particularly poor when the malignancy develops in the central nervous system (CNS), highlighting the complexity of this disease and the challenges in treating it.

Rituximab (RTX) has revolutionized the treatment of B-cell NHL. As a chimeric monoclonal antibody, RTX targets the CD20 antigen on B-cells, leading to their depletion. This mechanism has been effective in improving patient outcomes significantly when combined with standard chemotherapy regimens such as CHOP (cyclophosphamide, vincristine, doxorubicin, and prednisolone). However, despite its effectiveness, RTX faces limitations due to the development of treatment resistance. One primary mechanism of resistance is the loss of CD20 expression on malignant cells, which undermines RTX's ability to bind and exert its cytotoxic effects.

In addressing these challenges, researchers are exploring the combination of RTX with other therapeutic approaches, such as cancer vaccines. Cancer vaccines aim to induce a specific and long-lasting immune response against tumor antigens and current vaccines can be cell-based, protein/peptide-based, viral/bacterial-based, or gene-based. Each type has its advantages and limitations. For instance, cell-based vaccines are highly

immunogenic but difficult to mass-produce, while protein/peptide-based vaccines are easier to produce but have moderate immunogenicity.

To enhance the efficacy of cancer vaccines, adjuvants like Toll-like receptor (TLR) agonists are used to boost the immune response. TLR agonists can enhance the uptake and activation of dendritic cells, leading to a stronger T-cell response. Evidence suggests that RTX can generate a vaccinal effect by opsonizing tumor cells and targeting them for killing, thereby stimulating dendritic cells to present tumor antigens to T-cells. This process can create a durable anti-tumor response, complementing the direct cytotoxic effects of RTX as well.

The synergy between RTX and adoptive immunotherapy is particularly promising. Adoptive immunotherapy involves the transfer of tumor-specific T-cells into the patient, which can target and kill cancer cells more effectively. When combined with RTX, this approach can enhance the immune system's ability to recognize and attack B-cell lymphomas. RTX helps in the initial depletion of malignant B-cells, while adoptive immunotherapy provides a sustained immune response to prevent relapse.

In addition to immunotherapy, advancements in drug delivery systems are crucial for improving the treatment of NHL. Lymph nodes are critical in the metastatic spread of cancer and play a central role in initiating and regulating immune responses. Effective delivery of treatments to lymph nodes can enhance therapeutic outcomes and reduce the risk of metastasis and relapse. Thus, our approach is to develop nanocapsules for targeted delivery of therapeutic agents to lymph nodes.

Nanocapsules can encapsulate proteins or monoclonal antibodies, providing a protective shell that enhances stability and prolongs circulation time in the bloodstream.

By modifying these nanocapsules with targeting ligands such as MECA-79, which binds to PNAd expressed on high endothelial venules in lymph nodes, by which can achieve specific accumulation in lymph nodes. This targeted delivery ensures that therapeutic agents are concentrated where they are most needed, improving efficacy and reducing off-target effects.

In-vivo studies using murine lymphoma models have shown that MECA-79 modified nanocapsules can effectively inhibit tumor progression in both primary and metastatic tumor sites. These modified RTX nanocapsules lead to robust anti-lymphoma effects and demonstrate potential for inhibiting metastasis by eliminating remnant cancer cells in lymph nodes. This approach represents a significant advancement in the design of lymph-node targeting delivery platforms, addressing the limitations of current therapies.

Moreover, the adaptability of nanocapsules makes them suitable for personalized treatment strategies. By customizing the encapsulated cell strains in cancer vaccines or therapeutic agents in nanocapsules, therapeutic platforms can be tailored to meet individual patient needs. This flexibility is particularly valuable given the heterogeneity of lymphomas and the varying responses to treatment among patients.

The combination of RTX with cancer vaccines, adoptive immunotherapy, and nanotechnology-based delivery systems represents a comprehensive approach that leverages the strengths of passive and active immunity, offering new hope for patients with non-Hodgkin lymphoma.

Reference.

1. A. M. Badheeb, F. Ahmed, M. Elhadi, N. Alyami and M. A. Badheeb. Clinical and Therapeutic Profile of Non-Hodgkin's Lymphoma: A Retrospective Study From a Najran Oncology Center. *Cureus* **15**, e40125 (2023).
2. J. D. Hainsworth. Rituximab as first-line and maintenance therapy for patients with indolent non-Hodgkin's lymphoma: interim follow-up of a multicenter phase II trial. *Semin Oncol* **29**, 25-29 (2002).
3. R. P. Taylor and M. A. Lindorfer. Drug insight: the mechanism of action of rituximab in autoimmune disease--the immune complex decoy hypothesis. *Nat Clin Pract Rheumatol* **3**, 86-95 (2007).
4. F. Neumann, et al. Rituximab long-term maintenance therapy after autologous stem cell transplantation in patients with B-cell non-Hodgkin's lymphoma. *Ann Hematol* **85**, 530-534 (2006).
5. I. F. Khouri, et al. Concurrent administration of high-dose rituximab before and after autologous stem-cell transplantation for relapsed aggressive B-cell non-Hodgkin's lymphomas. *J Clin Oncol* **23**, 2240-2247 (2005).
6. Y. Kuroda, et al. Bone marrow stromal cell-mediated degradation of CD20 leads to primary rituximab resistance in mantle cell lymphoma. *Leukemia* **35**, 1506-1510 (2021).
7. Y. Jeon. Identifying and overcoming rituximab resistance in diffuse large B-cell lymphoma using next-generation sequencing. *Korean J Intern Med* **38**, 785-786 (2023).

8. M. E. Reff, et al. Depletion of B cells in vivo by a chimeric mouse human monoclonal antibody to CD20. *Blood* **83**, 435-445 (1994).
9. E. Oflazoglu and L. P. Audoly. Evolution of anti-CD20 monoclonal antibody therapeutics in oncology. *MAbs* **2**, 14-19 (2010).
10. T. A. Davis, et al. Rituximab anti-CD20 monoclonal antibody therapy in non-Hodgkin's lymphoma: safety and efficacy of re-treatment. *J Clin Oncol* **18**, 3135-3143 (2000).
11. G. J. Weiner. Rituximab: mechanism of action. *Semin Hematol* **47**, 115-123 (2010).
12. S. H. Lim, et al. Anti-CD20 monoclonal antibodies: historical and future perspectives. *Haematologica* **95**, 135-143 (2010).
13. E. C. Teo, Y. Chew and C. Phipps. A review of monoclonal antibody therapies in lymphoma. *Crit Rev Oncol Hematol* **97**, 72-84 (2016).
14. B. Coiffier. Effective immunochemotherapy for aggressive non-Hodgkin's lymphoma. *Semin Oncol* **31**, 7-11 (2004).
15. A. S. Michallet and B. Coiffier. Recent developments in the treatment of aggressive non-Hodgkin lymphoma. *Blood Rev* **23**, 11-23 (2009).
16. J. M. Foran, et al. Loss of CD20 expression following treatment with rituximab (chimaeric monoclonal anti-CD20): a retrospective cohort analysis. *Br J Haematol* **114**, 881-883 (2001).
17. J. H. Haidar, et al. Loss of CD20 expression in relapsed lymphomas after rituximab therapy. *Eur J Haematol* **70**, 330-332 (2003).
18. M. S. Czuczman, et al. Acquisition of rituximab resistance in lymphoma cell lines is associated with both global CD20 gene and protein down-regulation regulated at

- the pretranscriptional and posttranscriptional levels. *Clin Cancer Res* **14**, 1561-1570 (2008).
19. Y. Terui, et al. Identification of CD20 C-terminal deletion mutations associated with loss of CD20 expression in non-Hodgkin's lymphoma. *Clin Cancer Res* **15**, 2523-2530 (2009).
 20. Y. Xiao and D. Yu. Tumor microenvironment as a therapeutic target in cancer. *Pharmacol Ther* **221**, 107753 (2021).
 21. V. Chew, H. C. Toh and J. P. Abastado. Immune microenvironment in tumor progression: characteristics and challenges for therapy. *J Oncol* **2012**, 608406 (2012).
 22. Q. Gong, et al. Importance of cellular microenvironment and circulatory dynamics in B cell immunotherapy. *J Immunol* **174**, 817-826 (2005).
 23. M. Nakou, et al. Rituximab therapy reduces activated B cells in both the peripheral blood and bone marrow of patients with rheumatoid arthritis: depletion of memory B cells correlates with clinical response. *Arthritis Res Ther* **11**, R131 (2009).
 24. D. Baxter. Active and passive immunity, vaccine types, excipients and licensing. *Occup Med (Lond)* **57**, 552-556 (2007).
 25. S. Baris, et al. Efficacy of intravenous immunoglobulin treatment in children with common variable immunodeficiency. *J Investig Allergol Clin Immunol* **21**, 514-521 (2011).
 26. D. Baxter. Active and passive immunization for cancer. *Hum Vaccin Immunother* **10**, 2123-2129 (2014).

27. M. A. Keller and E. R. Stiehm. Passive immunity in prevention and treatment of infectious diseases. *Clin Microbiol Rev* **13**, 602-614 (2000).
28. T. M. Chucri, et al. A review of immune transfer by the placenta. *J Reprod Immunol* **87**, 14-20 (2010).
29. C. Quinello, W. Quintilio, M. Carneiro-Sampaio and P. Palmeira. Passive acquisition of protective antibodies reactive with *Bordetella pertussis* in newborns via placental transfer and breast-feeding. *Scand J Immunol* **72**, 66-73 (2010).
30. J. M. Bakker, W. K. Bleeker and P. W. Parren. Therapeutic antibody gene transfer: an active approach to passive immunity. *Mol Ther* **10**, 411-416 (2004).
31. G. Kumel, H. C. Kaerner, M. Levine, C. H. Schroder and J. C. Glorioso. Passive immune protection by herpes simplex virus-specific monoclonal antibodies and monoclonal antibody-resistant mutants altered in pathogenicity. *J Virol* **56**, 930-937 (1985).
32. C. Verwey and S. A. Madhi. Review and Update of Active and Passive Immunization Against Respiratory Syncytial Virus. *BioDrugs* **37**, 295-309 (2023).
33. H. Grubbs and C. I. Kahwaji. in *StatPearls* (Treasure Island (FL), 2024).
34. D. Song, et al. Passive and active immunity in infants born to mothers with SARS-CoV-2 infection during pregnancy: prospective cohort study. *BMJ Open* **11**, e053036 (2021).
35. T. Day, D. A. Kennedy, A. F. Read and S. Gandon. Pathogen evolution during vaccination campaigns. *PLoS Biol* **20**, e3001804 (2022).

36. N. Wang, et al. Vaccine-induced inflammation and inflammatory monocytes promote CD4⁺ T cell-dependent immunity against murine salmonellosis. *PLoS Pathog* **19**, e1011666 (2023).
37. C. F. Yung, et al. BNT162b2 vaccine induced variant-specific immunity, safety and risk of Omicron breakthrough infection in children aged 5 to 11 years: a cohort study. *Sci Rep* **13**, 17337 (2023).
38. S. Amara and V. Tiriveedhi. The Five Immune Forces Impacting DNA-Based Cancer Immunotherapeutic Strategy. *Int J Mol Sci* **18** (2017).
39. P. G. Coulie, B. J. Van den Eynde, P. van der Bruggen and T. Boon. Tumour antigens recognized by T lymphocytes: at the core of cancer immunotherapy. *Nat Rev Cancer* **14**, 135-146 (2014).
40. J. Martin-Liberal, et al. The expanding role of immunotherapy. *Cancer Treat Rev* **54**, 74-86 (2017).
41. N. Shang, et al. Dendritic cells based immunotherapy. *Am J Cancer Res* **7**, 2091-2102 (2017).
42. X. F. Zhang, et al. Dendritic-cell-based immunotherapy evokes potent anti-tumor immune responses in CD105⁺ human renal cancer stem cells. *Mol Carcinog* **56**, 2499-2511 (2017).
43. A. Perez-Banos, et al. Whole tumour cell-based vaccines: tuning the instruments to orchestrate an optimal antitumour immune response. *Br J Cancer* **129**, 572-585 (2023).

44. L. Diao and M. Liu. Rethinking Antigen Source: Cancer Vaccines Based on Whole Tumor Cell/tissue Lysate or Whole Tumor Cell. *Adv Sci (Weinh)* **10**, e2300121 (2023).
45. S. Y. Liu, et al. Nanoparticles-based multi-adjuvant whole cell tumor vaccine for cancer immunotherapy. *Biomaterials* **34**, 8291-8300 (2013).
46. M. Allahyari and E. Mohit. Peptide/protein vaccine delivery system based on PLGA particles. *Hum Vaccin Immunother* **12**, 806-828 (2016).
47. M. Neek, T. I. Kim and S. W. Wang. Protein-based nanoparticles in cancer vaccine development. *Nanomedicine* **15**, 164-174 (2019).
48. W. Li, M. D. Joshi, S. Singhanian, K. H. Ramsey and A. K. Murthy. Peptide Vaccine: Progress and Challenges. *Vaccines (Basel)* **2**, 515-536 (2014).
49. R. J. Malonis, J. R. Lai and O. Vergnolle. Peptide-Based Vaccines: Current Progress and Future Challenges. *Chem Rev* **120**, 3210-3229 (2020).
50. C. Larocca and J. Schlom. Viral vector-based therapeutic cancer vaccines. *Cancer J* **17**, 359-371 (2011).
51. A. Ulusoy and D. Kirik. Development of advanced therapies based on viral vector-mediated overexpression of therapeutic molecules and knockdown of disease-related genes for Parkinson's disease. *Ther Deliv* **2**, 37-50 (2011).
52. P. M. Arlen, et al. Clinical safety of a viral vector based prostate cancer vaccine strategy. *J Urol* **178**, 1515-1520 (2007).
53. X. Zhao, R. Zhao and G. Nie. Nanocarriers based on bacterial membrane materials for cancer vaccine delivery. *Nat Protoc* **17**, 2240-2274 (2022).

54. B. Toussaint, X. Chauchet, Y. Wang, B. Polack and A. Le Gouellec. Live-attenuated bacteria as a cancer vaccine vector. *Expert Rev Vaccines* **12**, 1139-1154 (2013).
55. A. Bringmann, S. A. Held, A. Heine and P. Brossart. RNA vaccines in cancer treatment. *J Biomed Biotechnol* **2010**, 623687 (2010).
56. M. A. McNamara, S. K. Nair and E. K. Holl. RNA-Based Vaccines in Cancer Immunotherapy. *J Immunol Res* **2015**, 794528 (2015).
57. K. Lundstrom. Latest development on RNA-based drugs and vaccines. *Future Sci OA* **4**, FSO300 (2018).
58. E. Faghfuri, et al. Recent developments of RNA-based vaccines in cancer immunotherapy. *Expert Opin Biol Ther* **21**, 201-218 (2021).
59. Y. F. Ma and Y. W. Yang. Delivery of DNA-based cancer vaccine with polyethylenimine. *Eur J Pharm Sci* **40**, 75-83 (2010).
60. A. Lopes, G. Vandermeulen and V. Preat. Cancer DNA vaccines: current preclinical and clinical developments and future perspectives. *J Exp Clin Cancer Res* **38**, 146 (2019).
61. B. Yang, J. Jeang, A. Yang, T. C. Wu and C. F. Hung. DNA vaccine for cancer immunotherapy. *Hum Vaccin Immunother* **10**, 3153-3164 (2014).
62. S. H. Lee, S. N. Danishmalik and J. I. Sin. DNA vaccines, electroporation and their applications in cancer treatment. *Hum Vaccin Immunother* **11**, 1889-1900 (2015).
63. B. Pulendran, S. A. P and D. T. O'Hagan. Emerging concepts in the science of vaccine adjuvants. *Nat Rev Drug Discov* **20**, 454-475 (2021).
64. T. Kawai and S. Akira. The role of pattern-recognition receptors in innate immunity: update on Toll-like receptors. *Nat Immunol* **11**, 373-384 (2010).

65. B. Beutler. Inferences, questions and possibilities in Toll-like receptor signalling. *Nature* **430**, 257-263 (2004).
66. L. A. O'Neill, D. Golenbock and A. G. Bowie. The history of Toll-like receptors - redefining innate immunity. *Nat Rev Immunol* **13**, 453-460 (2013).
67. C. Pifferi, R. Fuentes and A. Fernandez-Tejada. Natural and synthetic carbohydrate-based vaccine adjuvants and their mechanisms of action. *Nat Rev Chem* **5**, 197-216 (2021).
68. B. Pulendran. The varieties of immunological experience: of pathogens, stress, and dendritic cells. *Annu Rev Immunol* **33**, 563-606 (2015).
69. G. Cartron, H. Watier, J. Golay and P. Solal-Celigny. From the bench to the bedside: ways to improve rituximab efficacy. *Blood* **104**, 2635-2642 (2004).
70. D. J. DiLillo and J. V. Ravetch. Differential Fc-Receptor Engagement Drives an Anti-tumor Vaccinal Effect. *Cell* **161**, 1035-1045 (2015).
71. S. P. Hilchey, et al. Rituximab immunotherapy results in the induction of a lymphoma idiotype-specific T-cell response in patients with follicular lymphoma: support for a "vaccinal effect" of rituximab. *Blood* **113**, 3809-3812 (2009).
72. R. Abes, E. Gelize, W. H. Fridman and J. L. Teillaud. Long-lasting antitumor protection by anti-CD20 antibody through cellular immune response. *Blood* **116**, 926-934 (2010).
73. F. Nimmerjahn and J. V. Ravetch. Fcγ receptors as regulators of immune responses. *Nat Rev Immunol* **8**, 34-47 (2008).

74. K. Mihara, et al. Synergistic and persistent effect of T-cell immunotherapy with anti-CD19 or anti-CD38 chimeric receptor in conjunction with rituximab on B-cell non-Hodgkin lymphoma. *Br J Haematol* **151**, 37-46 (2010).
75. Q. Cheng, et al. CD20-specific chimeric antigen receptor-expressing T cells as salvage therapy in rituximab-refractory/relapsed B-cell non-Hodgkin lymphoma. *Cytotherapy* **24**, 1026-1034 (2022).
76. J. Wen, et al. Sustained delivery and molecular targeting of a therapeutic monoclonal antibody to metastases in the central nervous system of mice. *Nat Biomed Eng* **3**, 706-716 (2019).
77. A. Zhen, et al. HIV-specific Immunity Derived From Chimeric Antigen Receptor-engineered Stem Cells. *Mol Ther* **23**, 1358-1367 (2015).
78. G. E. Ringpis, et al. Engineering HIV-1-resistant T-cells from short-hairpin RNA-expressing hematopoietic stem/progenitor cells in humanized BLT mice. *PLoS One* **7**, e53492 (2012).
79. A. Zhen, et al. Stem-cell Based Engineered Immunity Against HIV Infection in the Humanized Mouse Model. *J Vis Exp* (2016).
80. J. Guo, et al. Cancer vaccines from cryogenically silicified tumour cells functionalized with pathogen-associated molecular patterns. *Nat Biomed Eng* **6**, 19-31 (2022).
81. M. K. Verma, et al. A novel hemolytic complement-sufficient NSG mouse model supports studies of complement-mediated antitumor activity in vivo. *J Immunol Methods* **446**, 47-53 (2017).

82. N. C. Sheppard, et al. Polyethyleneimine is a potent systemic adjuvant for glycoprotein antigens. *Int Immunol* **26**, 531-538 (2014).
83. Q. Tan, et al. Tumor-derived microparticles-based nanomaterial as platform for delivery of tumor antigens to enhance immunogenicity. *Chemical Engineering Journal* **464** (2023).
84. K. Hu, et al. An ocular mucosal administration of nanoparticles containing DNA vaccine pRSC-gD-IL-21 confers protection against mucosal challenge with herpes simplex virus type 1 in mice. *Vaccine* **29**, 1455-1462 (2011).
85. C. Rolfo, E. Giovannetti, P. Martinez, S. McCue and A. Naing. Applications and clinical trial landscape using Toll-like receptor agonists to reduce the toll of cancer. *NPJ Precis Oncol* **7**, 26 (2023).
86. S. Yi, et al. Tailoring Nanostructure Morphology for Enhanced Targeting of Dendritic Cells in Atherosclerosis. *ACS Nano* **10**, 11290-11303 (2016).
87. M. H. Teplensky, et al. Spherical Nucleic Acid Vaccine Structure Markedly Influences Adaptive Immune Responses of Clinically Utilized Prostate Cancer Targets. *Adv Healthc Mater* **10**, e2101262 (2021).
88. O. Chijioke, et al. Human natural killer cells prevent infectious mononucleosis features by targeting lytic Epstein-Barr virus infection. *Cell Rep* **5**, 1489-1498 (2013).
89. N. C. Walsh, et al. Humanized Mouse Models of Clinical Disease. *Annu Rev Pathol* **12**, 187-215 (2017).
90. M. W. Melkus, et al. Humanized mice mount specific adaptive and innate immune responses to EBV and TSST-1. *Nat Med* **12**, 1316-1322 (2006).

91. A. Rivera, X. Fu, L. Tao and X. Zhang. Expression of mouse CD47 on human cancer cells profoundly increases tumor metastasis in murine models. *BMC Cancer* **15**, 964 (2015).
92. M. Puchalapalli, et al. NSG Mice Provide a Better Spontaneous Model of Breast Cancer Metastasis than Athymic (Nude) Mice. *PLoS One* **11**, e0163521 (2016).
93. A. F. Chambers, A. C. Groom and I. C. MacDonald. Dissemination and growth of cancer cells in metastatic sites. *Nat Rev Cancer* **2**, 563-572 (2002).
94. F. Bray, et al. Global cancer statistics 2018: GLOBOCAN estimates of incidence and mortality worldwide for 36 cancers in 185 countries. *CA Cancer J Clin* **68**, 394-424 (2018).
95. I. J. Fidler. The pathogenesis of cancer metastasis: the 'seed and soil' hypothesis revisited. *Nat Rev Cancer* **3**, 453-458 (2003).
96. C. L. Chaffer and R. A. Weinberg. A perspective on cancer cell metastasis. *Science* **331**, 1559-1564 (2011).
97. K. W. Hunter, N. P. Crawford and J. Alsarraj. Mechanisms of metastasis. *Breast Cancer Res* **10 Suppl 1**, S2 (2008).
98. J. B. Wyckoff, J. G. Jones, J. S. Condeelis and J. E. Segall. A critical step in metastasis: in vivo analysis of intravasation at the primary tumor. *Cancer Res* **60**, 2504-2511 (2000).
99. D. W. Losordo and S. Dimmeler. Therapeutic angiogenesis and vasculogenesis for ischemic disease: part II: cell-based therapies. *Circulation* **109**, 2692-2697 (2004).
100. A. Dimberg. Chemokines in angiogenesis. *Curr Top Microbiol Immunol* **341**, 59-80 (2010).

101. L. Garnier, A. O. Gkoutidi and S. Hugues. Tumor-Associated Lymphatic Vessel Features and Immunomodulatory Functions. *Front Immunol* **10**, 720 (2019).
102. M. He, et al. Role of lymphatic endothelial cells in the tumor microenvironment-a narrative review of recent advances. *Transl Lung Cancer Res* **10**, 2252-2277 (2021).
103. M. X. Da, Z. Wu and H. W. Tian. Tumor lymphangiogenesis and lymphangiogenic growth factors. *Arch Med Res* **39**, 365-372 (2008).
104. A. Christiansen and M. Detmar. Lymphangiogenesis and cancer. *Genes Cancer* **2**, 1146-1158 (2011).
105. H. Deng, et al. Current Status of Lymphangiogenesis: Molecular Mechanism, Immune Tolerance, and Application Prospect. *Cancers (Basel)* **15** (2023).
106. P. Liu, et al. Lymphangiogenesis in gastric cancer: function and mechanism. *Eur J Med Res* **28**, 405 (2023).
107. P. S. Steeg. Tumor metastasis: mechanistic insights and clinical challenges. *Nat Med* **12**, 895-904 (2006).
108. J. B. Aragon-Ching and J. A. Zujewski. CNS metastasis: an old problem in a new guise. *Clin Cancer Res* **13**, 1644-1647 (2007).
109. S. Valastyan and R. A. Weinberg. Tumor metastasis: molecular insights and evolving paradigms. *Cell* **147**, 275-292 (2011).
110. D. Jones, E. R. Pereira and T. P. Padera. Growth and Immune Evasion of Lymph Node Metastasis. *Front Oncol* **8**, 36 (2018).
111. G. S. Mack and A. Marshall. Lost in migration. *Nat Biotechnol* **28**, 214-229 (2010).
112. L. Willis, et al. Breast cancer dormancy can be maintained by small numbers of micrometastases. *Cancer Res* **70**, 4310-4317 (2010).

113. M. G. Achen, G. B. Mann and S. A. Stacker. Targeting lymphangiogenesis to prevent tumour metastasis. *Br J Cancer* **94**, 1355-1360 (2006).
114. H. Qi, W. Kastenmuller and R. N. Germain. Spatiotemporal basis of innate and adaptive immunity in secondary lymphoid tissue. *Annu Rev Cell Dev Biol* **30**, 141-167 (2014).
115. R. Roozendaal, R. E. Mebius and G. Kraal. The conduit system of the lymph node. *Int Immunol* **20**, 1483-1487 (2008).
116. J. Komori, L. Boone, A. DeWard, T. Hoppo and E. Lagasse. The mouse lymph node as an ectopic transplantation site for multiple tissues. *Nat Biotechnol* **30**, 976-983 (2012).
117. H. Jiang, Q. Wang and X. Sun. Lymph node targeting strategies to improve vaccination efficacy. *J Control Release* **267**, 47-56 (2017).
118. M. Stanley. Potential mechanisms for HPV vaccine-induced long-term protection. *Gynecol Oncol* **118**, S2-7 (2010).
119. J. S. Turner, et al. SARS-CoV-2 mRNA vaccines induce persistent human germinal centre responses. *Nature* **596**, 109-113 (2021).
120. Y. H. Chung, V. Beiss, S. N. Fiering and N. F. Steinmetz. COVID-19 Vaccine Frontrunners and Their Nanotechnology Design. *ACS Nano* **14**, 12522-12537 (2020).
121. M. P. Manspeaker and S. N. Thomas. Lymphatic immunomodulation using engineered drug delivery systems for cancer immunotherapy. *Adv Drug Deliv Rev* **160**, 19-35 (2020).

122. S. Cai, Q. Yang, T. R. Bagby and M. L. Forrest. Lymphatic drug delivery using engineered liposomes and solid lipid nanoparticles. *Adv Drug Deliv Rev* **63**, 901-908 (2011).
123. P. Baluk, et al. Functionally specialized junctions between endothelial cells of lymphatic vessels. *J Exp Med* **204**, 2349-2362 (2007).
124. G. J. Randolph, V. Angeli and M. A. Swartz. Dendritic-cell trafficking to lymph nodes through lymphatic vessels. *Nat Rev Immunol* **5**, 617-628 (2005).
125. J. E. Moore, Jr. and C. D. Bertram. Lymphatic System Flows. *Annu Rev Fluid Mech* **50**, 459-482 (2018).
126. M. Y. Gerner, P. Torabi-Parizi and R. N. Germain. Strategically localized dendritic cells promote rapid T cell responses to lymph-borne particulate antigens. *Immunity* **42**, 172-185 (2015).
127. T. Junt, et al. Subcapsular sinus macrophages in lymph nodes clear lymph-borne viruses and present them to antiviral B cells. *Nature* **450**, 110-114 (2007).
128. A. Schudel, D. M. Francis and S. N. Thomas. Material design for lymph node drug delivery. *Nat Rev Mater* **4**, 415-428 (2019).
129. S. M. Grant, M. Lou, L. Yao, R. N. Germain and A. J. Radtke. The lymph node at a glance - how spatial organization optimizes the immune response. *J Cell Sci* **133** (2020).
130. A. Ager and M. J. May. Understanding high endothelial venules: Lessons for cancer immunology. *Oncoimmunology* **4**, e1008791 (2015).
131. L. Blanchard and J. P. Girard. High endothelial venules (HEVs) in immunity, inflammation and cancer. *Angiogenesis* **24**, 719-753 (2021).

132. S. D. Rosen. Ligands for L-selectin: homing, inflammation, and beyond. *Annu Rev Immunol* **22**, 129-156 (2004).
133. X. Bao, et al. Endothelial heparan sulfate controls chemokine presentation in recruitment of lymphocytes and dendritic cells to lymph nodes. *Immunity* **33**, 817-829 (2010).
134. S. T. Pals, D. J. de Gorter and M. Spaargaren. Lymphoma dissemination: the other face of lymphocyte homing. *Blood* **110**, 3102-3111 (2007).
135. L. Menzel, et al. Lymphocyte access to lymphoma is impaired by high endothelial venule regression. *Cell Rep* **37**, 109878 (2021).
136. P. R. Streeter, B. T. Rouse and E. C. Butcher. Immunohistologic and functional characterization of a vascular addressin involved in lymphocyte homing into peripheral lymph nodes. *J Cell Biol* **107**, 1853-1862 (1988).
137. D. Mohanan, et al. Administration routes affect the quality of immune responses: A cross-sectional evaluation of particulate antigen-delivery systems. *J Control Release* **147**, 342-349 (2010).
138. J. Weber, et al. Phase 1 trial of intranodal injection of a Melan-A/MART-1 DNA plasmid vaccine in patients with stage IV melanoma. *J Immunother* **31**, 215-223 (2008).
139. C. M. Jewell, S. C. Lopez and D. J. Irvine. In situ engineering of the lymph node microenvironment via intranodal injection of adjuvant-releasing polymer particles. *Proc Natl Acad Sci U S A* **108**, 15745-15750 (2011).
140. M. R. Rajebi, et al. Intranodal lymphangiography: feasibility and preliminary experience in children. *J Vasc Interv Radiol* **22**, 1300-1305 (2011).

141. T. Schwaab, et al. Clinical and immunologic effects of intranodal autologous tumor lysate-dendritic cell vaccine with Aldesleukin (Interleukin 2) and IFN-alpha2a therapy in metastatic renal cell carcinoma patients. *Clin Cancer Res* **15**, 4986-4992 (2009).
142. R. J. Barth, Jr., et al. A randomized trial of ex vivo CD40L activation of a dendritic cell vaccine in colorectal cancer patients: tumor-specific immune responses are associated with improved survival. *Clin Cancer Res* **16**, 5548-5556 (2010).
143. N. L. Trevaskis, L. M. Kaminskis and C. J. Porter. From sewer to saviour - targeting the lymphatic system to promote drug exposure and activity. *Nat Rev Drug Discov* **14**, 781-803 (2015).
144. G. M. Ryan, L. M. Kaminskis and C. J. Porter. Nano-chemotherapeutics: maximising lymphatic drug exposure to improve the treatment of lymph-metastatic cancers. *J Control Release* **193**, 241-256 (2014).
145. H. Wiig and M. A. Swartz. Interstitial fluid and lymph formation and transport: physiological regulation and roles in inflammation and cancer. *Physiol Rev* **92**, 1005-1060 (2012).
146. T. Stylianopoulos, et al. Diffusion of particles in the extracellular matrix: the effect of repulsive electrostatic interactions. *Biophys J* **99**, 1342-1349 (2010).
147. V. Bocci, G. P. Pessina, L. Paulesu and C. Nicoletti. The lymphatic route. VI. Distribution of recombinant interferon-alpha 2 in rabbit and pig plasma and lymph. *J Biol Response Mod* **7**, 390-400 (1988).
148. L. Feng, et al. Roles of dextrans on improving lymphatic drainage for liposomal drug delivery system. *J Drug Target* **18**, 168-178 (2010).

149. S. S. Wang, Y. S. Yan and K. Ho. US FDA-approved therapeutic antibodies with high-concentration formulation: summaries and perspectives. *Antib Ther* **4**, 262-272 (2021).
150. M. Yan, et al. A novel intracellular protein delivery platform based on single-protein nanocapsules. *Nat Nanotechnol* **5**, 48-53 (2010).
151. D. Xu, et al. Efficient Delivery of Nerve Growth Factors to the Central Nervous System for Neural Regeneration. *Adv Mater* **31**, e1900727 (2019).
152. M. Qin, et al. An Antioxidant Enzyme Therapeutic for COVID-19. *Adv Mater* **32**, e2004901 (2020).
153. R. Yan, et al. Enzyme Therapeutic for Ischemia and Reperfusion Injury in Organ Transplantation. *Adv Mater* **34**, e2105670 (2022).
154. X. Zhang, et al. Nanocapsules of therapeutic proteins with enhanced stability and long blood circulation for hyperuricemia management. *J Control Release* **255**, 54-61 (2017).
155. D. Wu, et al. A Bioinspired Platform for Effective Delivery of Protein Therapeutics to the Central Nervous System. *Adv Mater* **31**, e1807557 (2019).
156. A. Kusowska, et al. Molecular Aspects of Resistance to Immunotherapies-Advances in Understanding and Management of Diffuse Large B-Cell Lymphoma. *Int J Mol Sci* **23** (2022).
157. C. K. Lee, et al. Tumor metastasis to lymph nodes requires YAP-dependent metabolic adaptation. *Science* **363**, 644-649 (2019).